Directional Proton Conductance in Bacteriorhodopsin Is Driven by Concentration Gradient, Not Affinity Gradient

Zhong Ren

Department of Chemistry, University of Illinois at Chicago, Chicago, IL 60607, USA
Renz Research, Inc., Westmont, IL 60559, USA

zren@uic.edu
ORCID 0000-0001-7098-3127

Keywords
proton pump, retinal, serial crystallography, singular value decomposition, X-ray free electron laser

Abstract
It is widely spread that microorganisms can harvest energy from sun light to establish electrochemical potential across cell membrane by pumping protons outward. Light driven proton pumping against a transmembrane gradient entails exquisite electronic and conformational reconfiguration at fs to ms time scales. However, transient molecular events along the photocycle of bacteriorhodopsin are difficult to comprehend from noisy electron density maps obtained from multiple experiments when the intermediate populations coexist and evolve as a function of 13 decades of time. Here I report an in-depth meta-analysis of the recent time-resolved datasets collected by several consortiums. This analysis deconvolutes the observed mixtures, thus substantially improves the quality of the electron density maps, and provides a clear visualization of the isolated intermediates from I to M. The primary photoproducts revealed here suggest a proton transfer uphill against 15 pH units is accomplished by the same physics that governs the tablecloth trick. While the Schiff base is displaced at the beginning of the photoisomerization within ~30 fs, the proton stays due to its inertia. This affinity-independent early deprotonation builds up a steep proton concentration gradient that drives the directional proton conductance toward the extracellular medium. This mechanism fundamentally deviates from the widely adopted assumption based on equilibrium processes driven by light-induced changes of

proton affinities. The method of a numerical resolution of concurrent events from mixed observations is also generally applicable.

Introduction

Bacteriorhodopsin (bR) captures photon energy to pump protons outward from the cytoplasm (CP) against the concentration gradient, thus converts light into electrochemical energy. This integral membrane protein of 28 kDa singlehandedly achieves the exact same goal of photosynthesis and cellular respiration combined. This simplicity is widely exploited in optogenetics and bioelectronics (Fenno et al., 2011; Li et al., 2018). A trimeric form of bR on the native purple membrane shares the retinal chromophore and the same protein fold of seven transmembrane helices A-G (Fig. S1) with large families of microbial and animal rhodopsins (Ernst et al., 2014; Kandori, 2015). An all-*trans* retinal is covalently connected to Lys216 of helix G through a protonated Schiff base (SB) pointing toward the extracellular side (EC) in the resting state, of which the double bond C_{15}=N_{ζ} is also in *trans* (traditionally also noted as *anti* (McCarty, 1970)) Upon absorption of a visible photon, the retinal isomerizes efficiently and selectively to adopt the 13-*cis* configuration (Govindjee et al., 1990). Extensive structural events during the ultrafast isomerization sampling and stereochemical selection were recently revealed by the companion study of this work (Ren, 2021).

Photocycle

It has been shown that the species I or a collection of species prior to the photoisomerization arises before 30 fs and remains in 13-*trans* instead of a near 90° configuration about C_{13}=C_{14} (Zhong et al., 1996). A red-shifted intermediate species J in 13-*cis* forms around 450-500 fs and decays at 3 ps to a less red-shifted species K (Applebury et al., 1978; van den Berg et al., 1990), which lasts longer than five decades of time therefore becomes the most "stable" intermediate throughout the entire photocycle on a log-time scale. The blue-shifted L state emerges from K at 1-2 μs and converts to strongly blue-shifted M states at ~50 μs (Lozier et al., 1975). The L → M transition has been considered as the step for the proton acceptor, the carboxylate group of Asp85, to become neutralized by receiving a proton (Fahmy et al., 1992). This established view has been largely based on peak assignments in resonance Raman and Fourier transform infrared spectroscopy (FTIR) on wildtype bR and various mutants (Braiman et al., 1988, 1991; Gerwert et al., 1990; Lewis et al., 1974). However, the event

of SB deprotonation has been mistakenly inferred from the observed protonation of the carboxylate of Asp85. It has been widely quoted in the literature that the proton transfer from the SB to the proton accepter occurs as the M formation. This study finds that this proton transfer spans ten decades in time instead of a single event. The electron density maps of I to M are unscrambled from one another in this analysis. They clearly show extensive conformational changes leading to and developing from the isomerization of the chromophore (Fig. 1).

Structure

Although the first low resolution map of bR was revealed in 1975 (Henderson and Unwin, 1975), the majority of structural information awaited technology advances until the 1990s in cryo electron microscopy (Henderson et al., 1990), electron diffraction (Grigorieff et al., 1996), and X-ray crystallography (Pebay-Peyroula et al., 1997). Finally, the atomic resolution of a bR model was achieved (Luecke et al., 1999a). The main technique to study intermediates along the photocycle used to be cryo trapping, including both light illumination of crystals at room temperature followed by rapid freezing and illumination at elevated cryo temperatures. The 13-*cis* retinal and its associated H-bond network have been observed in M state with extensive conformational changes in the anchor helix G (Luecke et al., 1999b), FG loop, EC half of helix C (Takeda et al., 2004), and an enlarged CP pocket (Sass et al., 2000). Numerous attempts have been made to capture intermediates other than M with inconsistent results (Wickstrand et al., 2015).

A new phase began with time-resolved serial crystallography conducted at X-ray free electron lasers (XFELs). The ultrashort X-ray laser pulses open the opportunity to capture transient structural species in the photocycle as short-lived as fs. It is equally important that serial crystallography enables photo triggering and data collection at room temperature. Authentic signals of conformational changes of greater amplitudes are expected at room temperature compared to cryo trapping. Several international consortiums carried out large operations and accumulated abundant time points along the photocycle that spans more than 13 decades of time. Judged only from the extensiveness of the reported signals, time-resolved XFEL data at room temperature unfortunately do not surpass those captured by cryo trapping, which hints at much needed improvements in experimental protocols and data analysis methods. Nogly et

al. captured retinal isomerization to 13-*cis* at 10 ps (Nogly et al., 2018). More importantly, they observed that the SB water moves before the isomerization and the SB itself has already displaced at the earliest time point of 49-406 fs, which is the key contribution to this analysis. Kovacs et al. contributed datasets at many short time delays (Kovacs et al., 2019). Nango et al. found an ordered water in a newly established H-bond network involving the SB in the 13-*cis* retinal pointing to the CP on ns-μs time scale, which led to their conclusion of the proton path (Nango et al., 2016). These are three major sources of data analyzed in this study (Table S1). Several synchrotron datasets at ms delays also contribute to this analysis (Weinert et al., 2019).

Structural heterogeneity is the common difficulty to both cryo trapping and time-resolved serial crystallography at room temperature. To what extend a specific species can be enriched in crystals depends on the reaction kinetics under a condition of illumination, such as wavelength and temperature. A more stable species K or M can reach a higher fractional concentration at a specific time point due to a greater ratio between the rates going into and exiting from that species. Others will be populated poorly because of their transient nature. This structural heterogeneity causes the practical difficulties in the interpretation of electron density maps and the refinement of these intermediate structures (Ren et al., 2013). An assumption in nearly all previous studies has been that each dataset, at a cryo temperature or at a time delay, is derived from a mixture of a single photoinduced species and the ground state. Therefore, the difference map reveals a pure intermediate structure. This assumption leads to the more time points the more overinterpretation rather than the more overdetermination. Previous studies using cryo trapping and time-resolved crystallography could not evaluate clear electron density maps of pure intermediate species without a proper deconvolution of heterogeneous species. Because none of the experimental conditions at a cryo temperature or a time point can guarantee an experimental map that does not involve heterogeneous mixture (Ren et al., 2013; Yang et al., 2011). This work is yet another case study to test our general strategy of dynamic crystallography, that is, from the outset every observation at a time point or a temperature setting is treated as a mixture of unknown number of structural species with unknown populations (Methods). The structures of all intermediate species are also unknown except the ground state. The analytical protocol is responsible for a reliable structural interpretation by overdetermination of these unknowns from consistent observations

(Ren, 2019; Ren et al., 2013; Yang et al., 2011). Inconsistent observations are identified and isolated.

Mechanism

Understanding the mechanism of proton pumping uphill against gradient has been centered on two entangled aspects: Where are the proton uptake and release pathways? How does the retinal photoisomerization adjust the chemical groups' ability to hold proton along these pathways? The ability of a chemical group to hold a proton is measured by its value of pK_a, where p stands for -$\log_{10}$ function and K_a is the acid dissociation constant, one form of the equilibrium constant of a chemical reaction. It is clear that a proton previously retained by the SB is accepted by the carboxylate group of Asp85 in helix C and eventually released to the EC medium. Each of Arg82, Asp85, 212, Glu194, 204, and some waters could play a role (Balashov et al., 1997; Govindjee et al., 1996; Richter et al., 1996). However, the sequence of events during this proton conductance is unclear thus often mistakenly inferred.

At the resting state of bR, the SB holds a proton tightly with a pK_a of 13.3 pointing toward the EC channel (Druckmann et al., 1982; Sheves et al., 1986). The nearby proton acceptor Asp85 bridged to the SB by a water stays quite acidic with its pK_a spanning 2-3 range (Balashov et al., 1996). That water, often numbered as 402, has been identified as the centerpiece of the mechanism (Wickstrand et al., 2015). Therefore, the SB proton is associated with both N and O simultaneously in N_ζ:H^+:OH_2 with both interactions much weaker than an ordinary single bond (Fig. 2c). One of the competing hypotheses is willing to consider that the proton is first brought to the CP side by the SB isomerization to 13-*cis*, and then conducted through Thr89 and a newly found water other than Wat402 on the CP side, and finally reaches Asp85 (Nango et al., 2016). The difficulty encountered by this hypothesis is the rollercoasting pK_a values that the proton has to go through. The other competing hypothesis relies on a H-bond network long after photoisomerization but largely similar to that in the resting state to translocate the proton on the SB. The H-bond from the SB to Wat402 has to be reconciled with two double bonds C_{13}=C_{14} and C_{15}=N_ζ, both highly twisted away from *trans* and *cis* configurations to near 90°, until a successful proton translocation to Asp85 (Lanyi and Schobert, 2007). This interpretation of these highly twisted double bonds is a direct

consequence of the inability to unscramble a mixed observation of multiple conformations.

Despite intense studies, fundamental questions on the operating mechanism of this proton pump remain puzzling and some unanswered. Q1) How does the protonated SB with a pK_a of 13.3 transfer its proton to the acidic acceptors and when? Q2) Which molecular event, the isomerization, or another event, switches the accessibility of the SB from EC to CP and how does the SB avoid reprotonation on the wrong side? Q3) How are protons conducted > 15 Å through the rollercoasting pK_a values and released into the EC medium from the SB of a high pK_a through aspartic acids of low pK_a, arginine (strictly speaking, its guanidinium ion) and tyrosines of high pK_a, and glutamic acids of low pK_a again? Q4) How is a gradient-driven proton backflow prevented in the resting state and during the pumping motions? No convincing evidence can directly demonstrate a photoinduced reversal of the drastically different proton holding abilities along the EC half channel to facilitate a spontaneous proton conductance that would require an ascending order of pK_a's. The fundamental flaw in the previous line of thinking is multiple equilibrium steps driven by proton affinities as the values of pK_a describe. A proton is spontaneously transferred from one chemical group with a less proton affinity, that is, smaller pK_a, to another with a greater affinity, that is, larger pK_a (Jardetzky, 1966; Stoeckenius et al., 1979). Such proton conductance was presumed to be accomplished by the means of abundant thermal events of protonation and deprotonation, that is, equilibrium. If a slope of affinity does not satisfy the directional flow of protons, it has been commonly assumed that a photoinduced reversal of proton affinity must have occurred during the photocycle (Stoeckenius, 1999). This study shows that equilibrium is not how the light-driven proton pump bR works, and the directional proton conductance is not driven by increasing affinities but by a concentration gradient of protons.

Here the ultrafast molecular events revealed from the serial crystallographic datasets demonstrate that the photochemical reaction of bR transfers a proton held by the SB to form a strong acid that barely has any ability to hold a proton. However, this proton transfer is not achieved by equilibrium therefore not governed by pK_a's. Instead, before the isomerization occurs, this proton transfer takes place due to the SB displacement within ~30 fs in a single molecular event. The proton's inertia prevents it

from accelerating as fast as the SB under the same physics of the tablecloth trick (Q1). Rapid photoisomerization flips the already deprotonated SB at 500 fs, thus protects the SB from being reprotonated on the wrong side (Q2). Proton conductance follows a descending order of the proton concentration gradient established in the EC half channel (Q3). A built-in seal constructed by an irregular helix reacts to the isomerization and ensures no proton leakage back to the CP channel during the motions of proton pumping (Q4). The inner EC channel is strictly surrounded by chemical groups of high pK_a's so that protons can only flow out but cannot flow back in even during dark (Q4). See Supplementary Information (SI) for coherent answers to these questions.

Results and Discussion

A total of 42 datasets and 36 time points analyzed in this study are divided into two groups: 18 short delays up to 10 ps and 18 long delays ranging from ns to ms, which unfortunately leaves a gap longer than three decades not surveyed (Fig. 1 and Table S1). Difference Fourier maps among these time points and with respect to their corresponding dark datasets are calculated according to protocols previously described (Methods). Singular value decomposition (SVD) of difference maps and the subsequent Ren rotation in a multi-dimensional Euclidean space established by SVD (Ren, 2016, 2019, 2021) are performed separately to 126 difference maps of the short delays and 101 maps of the long delays (Methods). This method of "decomposition and deconvolution" results in a clean separation of electron density changes due to coexisting photoexcited species mixed in the observed datasets. The main findings are summarized in a Gantt chart (Fig. 1). Eight intermediate structures along the photocycle, now isolated from one another, are refined against reconstituted structure factor amplitudes (Methods; Table S2) (Ren, 2021). The assignments of the previously identified intermediates I to M to these refined structures are largely based on the time stamps of the observed signals. No absorption signatures are directly associated with the X-ray data.

Intermediates I′, I, and Schiff base deprotonation

Three decomposed map components $\boldsymbol{U}_{10}$, $\boldsymbol{U}_{14}$, and $\boldsymbol{U}_{17}$ of the short delays contain extraordinary structural signals in terms of their extensiveness and quality (Ren, 2021). These signals originate exclusively from a few time points of Nogly et al., too few to fit

the time dependency with exponentials. Instead, a spline fitting through these time points estimates the coefficients c_{10}, c_{14}, and c_{17} in the linear combination of $c_{10}\boldsymbol{U}_{10} + c_{14}\boldsymbol{U}_{14} + c_{17}\boldsymbol{U}_{17}$ for the early states I, J, and their respective precursors I′, J′ (Ren, 2021). The precursor prior to I state is located on the spline trajectory from the origin, that is, the ground state bR at the time point of 0- before the photon absorption, to the first time point of 49-406 fs (PDB entry 6g7i). It would be appropriate to name this location on the trajectory I′ as a precursor leading to I state judged only by the time point at ~30 fs.

The all-*trans* retinal in bR is largely flat except C_{15} (Fig. 2b 2nd panel). However, two single bonds of Lys216 are highly twisted to near 90° (Fig. 2b 4th panel), which forms a corner at C_{ε} that deviates from the flat plane of the all-*trans* retinal, protrudes inboard, and makes a van der Waals contact at 3.4 Å with Thr89 in helix C (Fig. 2b 2nd panel). This contact is identified in this study as a seal between the extracellular (EC) and cytoplasmic (CP) half channels. The retinal in I′ remains in near perfect all-*trans* configuration, including the Schiff base (SB) double bond C_{15}=N_{ζ} (Fig. S2), while it is creased into an S-shape in an expanded retinal binding pocket together with other features revealing the isomerization sampling (Ren, 2021). The slit between Thr89 and the SB increases to 4.3 Å that may break the seal between two half channels, which is inconsequential as argued below. The C_{20} methyl group swings 1.1 Å to the outboard direction, a motion previously known but at much later time. These motions are rotations around the long axis of the polyene chain instead of translations (Fig. 2b bottom panel). It is important that the displaced Wat402, now a hydronium ion H_3O^+ (see below), remains H-bonded to both Asp residues in I′. However, its association with the SB increases to 3.3 Å that barely qualifies as a H-bond.

Due to the availability of the time stamp, a conformational change captured in a time-resolved experiment can be converted to the velocity of an atomic displacement that would further hint the acceleration and force required to achieve the observed conformation changes at the time of the measurement. It can be shown that a force > 500 pN is required to keep the proton accelerating as fast as N_{ζ} that has been displaced by 0.7 Å within 30 fs. This is not achievable given the charge on the proton and its H-bond association with Wat402. Compared to the regular single bond N-H in an amine group at a pK_a of 40, the coordination bond N_{ζ}:H^+ in the protonated SB at its pK_a of 13.3 is much weaker. In addition, a proton acceleration with the SB would have to break its

interaction with Wat402, nearly as costly as to break the coordination bond N_ζ:H^+ (Fig. 2c). Therefore, which of the two weak interactions N_ζ:H^+:O402 survives the abrupt tare before the photoisomerization is determined by the inertia of the proton. I′ captures the starting moment of a reliable deprotonation from the SB that does not depend on thermal equilibrium. Here the 0.6 Å increase from the SB to Wat402 is attributed to the separation of the proton from the SB rather than from Wat402. Instead of accelerating with the SB, the proton stays with Wat402 to form a hydronium H_3O^+ due to its inertia (Q1; Figs. 1 inset and 2c). Since several water molecules have been observed in the inner EC channel, possibilities of other proton complexes also exist, such as $H_5O_2^+$ (Marx et al., 1999; Mathias and Marx, 2007). The hydronium 402 has been shown possible by magic angle spinning NMR (Friedrich et al., 2020).

This conjecture here, however, is not based on an observation of the scattered X-rays by the proton as the proton does not scatter X-ray. Direct evidence supporting this water cluster with excess protons reside in FTIR observations. Complex kinetic behaviors of several broad band continua at the frequencies > 1700 cm^{-1} were recorded in FTIR experiments and interpreted as protonated water clusters (Garczarek et al., 2004, 2005; Lorenz-Fonfria et al., 2017; Wang and El-Sayed, 2001). However, detailed assignments of these continua remain debatable. For example, the removal of one terminal carboxylate near the exit of the EC channel (Fig. S1) in the mutant E204Q certainly could affect proton release. But the observed change in some FTIR continua cannot be easily pinpointed to a water cluster in the outer EC channel (Garczarek et al., 2004), since shutting down one proton release pathway could affect the kinetics of the upstream water cluster in the inner EC channel. Furthermore, the FTIR continua most likely originate from a super-acidic water cluster in the inner EC channel because a well-known proton barrier surrounds the inner EC channel but no proton barrier for the outer EC channel (see below).

The hydronium 402 is likely short-lived. Either Asp85 or 212 “quickly” accepts another proton from the hydronium and returns it back to Wat402 (Fig. 1 inset). The lifetime of hydronium 402 is unclear from X-ray diffraction. Nevertheless, this lifetime does not have to contradict the commonly adopted view that these aspartic acids are protonated later in tens of μs to ms during M formation (Braiman et al., 1988, 1991; Gerwert et al., 1990), given that the pK_a difference between the aspartic acid and

hydronium is < 4 pH units. As argued below, a super-acidic water cluster harboring excess protons in the inner EC channel must be established before proton release. Reliable deprotonations from the SB in consecutive photocycles continuously overcharge the inner EC channel. The deprotonation event cannot be directly inferred from the vibrational signatures due to the protonation of the carboxylic proton acceptors in the Asp residues. In other words, the "proton transfer" from the SB to the proton acceptor, as commonly stated in the literature, is not a single event. Instead, it spans ten decades in time.

The retinal in I state remains in near perfect all-*trans*, including the SB. However, the major difference from the precursor is that the single bond N_ζ-C_ε is now in a perfect *syn* conformation, and the anchor Lys216 has largely returned to its resting conformation (Figs. 2b 4th panel and S3). The SB makes a sharp U-turn toward inboard before 500 fs (Fig. S2) and closes the slit with Thr89 to 3.8 Å and ends the breakage in the seal that is too brief to result in a proton leakage (Q3). After the U-turn, the deprotonated SB is pointing toward inboard while Wat402, currently a hydronium, is displaced outboard but remains H-bonded to both Asp85 and 212. The SB and Wat402 are not only beyond a H-bond distance, but also in a bad geometry for proton exchange (Fig. S3d). The accessibility of the SB in I state is already very limited while the SB is reoriented toward inboard despite that the isomerization is yet to occur (Q2). This ultrafast U-turn is how the SB gets rid of the proton by a mechanism of the same physics that governs the tablecloth trick (Q1; Fig. S2). Holding Wat402 in place by Asp85 and 212 symmetrically from inboard and outboard, respectively, is as important as the ultrafast shaking of the SB to its successful deprotonation. See SI for mutant functions when the symmetric holding of Wat402 is disrupted. Here the tablecloth trick is not an analogy to the SB deprotonation. Both are governed by the exact same Newton mechanics: A certain mass, such as a planetary body, a dinning set, or a proton, does not accelerate fast enough unless a sufficient force is exerted on it. The U-turn of the SB marks the peak power, or the maximum rate of enthalpy change dH/dt, of the entire photochemical reaction (see Discussion). The spectrogram derived from the transient absorption or transmittance clearly supports that the photocycle reaches its peak power within the first tens of fs (Kahan et al., 2007; Kobayashi et al., 2001). If a deprotonation is unsuccessful at the peak power of the photocycle, there will be no further opportunity to translocate a proton from a fair base to a decent acid uphill

against 11 pH units under equilibrium. The same is true that a proton transfer is energetically impossible from the protonated SB at a pK_a of 13.3 to form a hydronium, a strong acid of a pK_a of -1.7, under equilibrium. The deprotonated SB is extremely vulnerable at this moment in I state despite its limited accessibility, as it will be quickly reprotonated if it lingers on in the EC channel to allow an equilibrium. As shown below, the isomerization to a 13-*cis* retinal prevents such an equilibrium in a futile photocycle. However, some of the photocycles are indeed unsuccessful as its quantum yield indicates if a reprotonation event does occur before the isomerization.

Incidentally, all previous hypotheses on the mechanism of SB deprotonation imply a formation of hydronium at one point or another (Lanyi and Schobert, 2007; Nango et al., 2016). It would require a donor group with a pK_a more negative than -1.7 to reliably form a hydronium by the means of equilibrium. None of the previous hypotheses have successfully explained how this is possible.

Intermediates J′, J and traveling water or hydronium 402

Near perfect 13-*cis* is successfully refined in both structures of J′ at ~700 fs and J at ~20 ps with a contracted retinal binding pocket (Fig. 2b 4th panel) (Ren, 2021). However, the SB double bond C_{15}=N_ζ is momentarily distorted from the *trans* configuration in J′ with a torsion angle of 133°. The *trans* double bond C_{15}=N_ζ is promptly restored in J (Fig. 2b 4th panel). The SB N_ζ is rotating clockwise looking from the proximal to distal direction in the entire process of the isomerization I′ → I → J′ → J (Fig. 2a). If the deprotonated SB isomerizes to 13-*cis* at ~500 fs, this photocycle is productive. Otherwise, a photocycle could be wasted if reprotonation occurs prior to the isomerization as it could happen sometimes even in wildtype. The isomerization completes the accessibility switch for the SB from the EC half channel to the CP (Q2).

Due to the 13-*cis* configuration, C_{20} methyl group protrudes to a CP direction that is further tilted toward outboard from its original direction. No additional consequence is immediately obvious until the retinal flattens and returns to its original plane at later intermediates. At this moment, Trp182 and the retinal anchor Lys216 stay in their resting positions. Wat402, perhaps currently still a hydronium ion, is well defined in both Js (Ren, 2021). Contrary to the previous conclusion (Wickstrand et al., 2015), this traveling water is never disordered throughout the surveyed portion of the photocycle

up to M_2 (see below) despite its large trajectory spanning greater than 3 Å (Fig. 2a). Wat402 is observed with both strong difference electron density and its refined electron density. Its association with Asp85 and 212 remains unwavering throughout the photocycle except one increase to 4.1 Å from Asp212 during J′, the first moment after isomerization. This observation demonstrates that Wat402, a hydronium through a large part of the photocycle, is an integral part of the moving cluster that accepts the proton from the SB. Most likely, this water will remain ordered throughout the rest of the photocycle not yet surveyed.

The main cause to this contradiction is that a light induced change at any given time point consists of a mixture of multiple conformations. As the most straightforward example, the dramatic motion of Wat402 appears to be a disorder in an experimental map prior to deconvolution. An experimental map is a spatial average over the diffracting crystals and a temporal average over the X-ray exposures. In case of serial crystallography, the range of this average is an extensive pool of crystals potentially with diverse individualities (Ren et al., 2018). The only common feature among multiple species of bR intermediates is the negative density on the original location of Wat402 due to its departure. Multiple positive features at various locations are of low occupancies without a proper deconvolution. In this analysis, a linear combination of several SVD components unscrambles the mixture so that each state along the photocycle presents a pure conformational species, a time-independent structure. Is there an experimental solution to this problem of structural heterogeneity? Would a better time resolution improve an experimental difference map so that a traveling water molecule would always be temporally resolved? The answer is both surprisingly and conclusively no, even if, for the sake of argument, an ultimate time resolution of truly zero is achievable by two zero-width impulses of pump and probe (Strictly speaking, each crystal must also be a spatial impulse, that is, zero size.). Because at no time throughout the entire photocycle, the traveling water is synchronized throughout the entire crystal, even if every retinal in the crystal absorbs a visible photon at the exact same time zero. There is no difference between crystal and solution in this aspect, which has been long recognized as Moffat laid the foundation of time-resolved crystallography (Moffat, 1989, 2001). In conclusion, a numerical resolution of structural heterogeneity, as exemplified here, is the last and the only resort (Ren et al., 2013).

Five-decade long-lived K and global change in L

This work continues with another joint analysis of the time-resolved datasets at long delays > 10 ns collected mainly by Nango et al. with contributions from Nogly et al., Kovacs et al., and Weinert et al. (Table S1). These datasets at the long delays are relatively noisier and contain systematic errors from one experiment to another. The analytical procedure of SVD and the subsequent Ren rotation (Ren, 2016, 2019, 2021) is capable of isolating time-resolved signals from these error and noise components. SVD of 101 difference Fourier maps identifies 19 major components (Fig. S4a). Four of them contain outstanding signals of structural changes (Fig. S5). Two others also carry structural signals but without a clear time dependency (Fig. S6). The number of datasets at long delays warrants an exponential fitting to the SVD coefficients (Fig. S7) (Schmidt et al., 2010), which models the reaction scheme of the photocycle better compared to the spline fitting applied to the limited number of short delays above. The time constants obtained from the exponential fitting agree well with the transition times between intermediates K, L, M_1, and M_2 known from spectroscopy. Coefficients for relatively pure states are estimated and the refinement protocol based on reconstituted difference maps again produce atomic coordinates of these states (Methods) (Ren, 2021).

The refined structures of K and L are discussed in SI (Figs. S8 and S9). A flattened 13-*cis* retinal is finally achieved in L with many global changes. The L state represents the end goal of the global conformational changes due to the retinal isomerization. Additional changes after L are no longer global (see below). C_δ-C_ε of the anchor moves outboard and could break the seal with Thr89 once again. Last time, a potential breakage occurs in I′ at tens of fs that is too brief for any proton leak (Fig. 2b 2nd panel). This time, the ns-μs time scale allows the protein to react. It is clearly observed that Thr89 and helix C always follow C_δ-C_ε outboard in J, K, and L and maintain a distance no more than 3.6 Å because of its tendency to be straightened (Figs. 3f and S10a). This motion was also captured previously in cryo-trapped intermediates (Royant et al., 2000). Therefore, the seal between two half channels is kept intact (Q4). Here the mechanism of these motions of helices is attributed to several irregularities in these helices (Fig. S10), the kinked helix C (Grigorieff et al., 1996), the stretched helix F, and the π helical segment in G (Pebay-Peyroula et al., 1997). Contrary to the previous belief (Luecke et al., 1999a), it is our general conclusion also from studies of other protein mechanisms that irregularities in secondary structures not merely fulfill some structural

requirements but offer a wide variety of mechanical properties to achieve the functions of protein nanodevices (Ren et al., 2016; Shin et al., 2019). These motions of the helical segments collectively result in a tighter EC channel and an open CP channel in L (Fig. S11).

Intermediates M_1, M_2 and proton release

The refined structures of M_1 and M_2 are described in SI (Figs. S12 and S13). Thr89 is kept 3.1 Å away from the SB in L, M_1, and M_2 constantly so that the seal is well maintained between two half channels (Q4). Compared to the slightly longer distance between Thr89 and the SB at 3.6 Å in J and K, it is obvious that Thr89 and helix C react to the retreating SB during J and K, but the SB is actively pushing Thr89 and helix C from L to M (Fig. 4c). As discussed below, during pumping activity, drastic proton concentration gradient is present across this seal that divides two half channels. A well-maintained seal is crucial to the efficiency of the pump. Various mutants with substitutions of Thr89 that could result in a proton leak retain ~2/3 of the pumping activity compared to the wildtype (Marti et al., 1991).

The motions over the EC half of the molecule from tens of μs to ms are directly related to the pathway of the proton release (Q3). Residues in the EC half channel are not arranged in a monotonic order of their pK_a's. Quite the contrary, acidic residues Asp85 and 212 with the smallest pK_a's are at the end of the half channel next to the SB with the greatest pK_a. Another layer of acidic residues Glu9, 194, and 204 are at the EC surface. It is puzzling that Arg82, Tyr57, and 83 are located between these two acidic layers (Figs. 5 and S1). It had been depicted multiple times by similar illustrations in the past that a high pK_a layer is sandwiched between two acidic layers with low pK_a's in the EC half channel. Yet, the question remains: How are protons conducted through the proton barrier of the guanidinium group of Arg82 that is already protonated and the phenol hydroxyl groups of the Tyr residues that cannot be protonated anymore (Brown et al., 1993)? No evidence shows that such rollercoasting pK_a values would change in any meaningful way by the light-induced conformations. Therefore, the previous proposal on an affinity-driven proton conductance is fundamentally flawed.

Proton conductance after SB deprotonation through the EC half channel not necessarily operates on the basis of one event of proton release per photocycle. It was

previously suggested that a proton pumped in one photocycle could be released in the next or subsequent photocycles (Braiman et al., 1991). However, a flawed common assumption persists that the pumping and releasing of each proton are somehow scheduled in different periods of a photocycle. Here a concentration-driven, instead of affinity-driven, proton conductance is hypothesized. Proton release becomes synchronized to the photocycle only when a super-acidic inner EC channel is established. The first a few photocycles build up a proton concentration at the end of the EC half channel. Multiple groups in the inner EC channel, including various waters, could be all protonated after consecutive photocycles, that is, a puddle of protons establishes a super-acidic inner EC channel as long as the seal of Thr89 is well maintained. This is possible because the proton pumping step is a physical process instead of a chemical equilibrium (see above). Although the first a few photocycles are productive, they are not capable of releasing any proton before an established proton concentration gradient. An established super-acidic inner EC channel triggers a concentration-driven proton conductance. Proton release from the wildtype bR was observed before proton uptake as if it is coupled with, if not faster than, the protonation of the proton acceptor Asp85 (Braiman et al., 1988, 1991; Gerwert et al., 1990; Zimanyi et al., 1992), which strongly suggests that the newly pumped proton is not the one released to the EC medium in the same photocycle. Here the concentration-driven proton conductance argues that the newly pumped proton causes a proton overflow from the already super-acidic inner EC channel. Therefore, the observed "early release" is actually a very late release during a subsequent photocycle, several cycles after the very proton has been pumped into the inner EC channel.

The inner EC channel has been called a proton cage at the active site of bR (Friedrich et al., 2020), which reflects the same fact of the proton barrier (Fig. 5). Here I argue that the super-acidic inner EC channel causes a second protonation of the guanidinium group because of three electron-rich nitrogens. The observation to corroborate this speculation is the motions of Arg82, Glu194, and 204 during K → L → M_1 → M_2. The monovalent guanidinium cation during the early photocycle has no salt bridge to Glu194 and 204 until M state. It appears that Asp85 and 212 are continuously protonated by proton pumping thus neutralized in the inner EC channel. Several hydronium ions make the inner EC channel positively charged. The observed kinetics of FTIR continua could explain excess protons harbored by the water cluster in the

inner EC channel (Garczarek et al., 2004, 2005; Lorenz-Fonfria et al., 2017; Wang and El-Sayed, 2001). An extra positive charge on the short-lived divalent guanidinium in M drives itself away from the inner EC channel and toward the negative charged Glu residues in the outer EC channel (Fig. 5a). The EC segments of helices C and G move closer to each other in the refined M structures, where Arg82 is sandwiched in between (SI; Fig. 4). Molecular dynamics simulations found that the orientation of Arg82 is correlated with the charge difference between the inner and outer acids (Ge and Gunner, 2016). The contact among Glu194, 204, and the guanidinium discharges the extra proton to the outer EC channel and the EC medium. A monovalent guanidinium cation is unable to discharge its proton to the carboxylates of the Glu residues due to their low proton affinity. Therefore, Arg82 is a unidirectional proton valve that conducts protons outward, but only under sufficient proton concentration in the inner EC channel. During dark, Arg82 prevents a concentration-driven proton leak back into the cell, because the EC medium cannot become super acidic as long as sufficient water is available. See SI for mutant functions when the proton barrier is breached by substitutes for Arg82.

Discussion

Under the guidance of Jardetzky's allostery model of transmembrane pump (Jardetzky, 1966) and the common line of thinking led by Stoeckenius (Stoeckenius et al., 1979), evidences were sought in the past half century to explain how the absorbed photon energy is used to alter the proton affinity landscape along its pathway so that protons can flow in one direction along an ascending order of pK_a values. Neither a hydraulic powered noria or an animal powered sakia in the old time, nor an electric powered fluid pump in the modern days, works under such an operating principle that requires energy for a reconstruction of the landscape. Quite the contrary, the landscape is a given constant and energy is absorbed by the to-be-pumped substance to gain its potential energy, such as water is lifted by a noria or pressurized by an electric pump. The energized substance will then flow freely along the largely constant landscape governed by thermodynamics. In the meanwhile, it is critical to prevent a backflow along a far more steep gradient than the forward-driving gradient. The molecular pump bacteriorhodopsin (bR) for protons works under the exact same principle that fundamentally differs from what Jardetzky and Stoeckenius once imagined. Other transmembrane molecular pumps and transporters likely work the same way at this

544 philosophical level disregarding any molecular detail. Alteration of affinities to the
545 pumped substance cannot be an effective strategy because it is against the chemical
546 nature along the translocation pathway and therefore energetically difficult to achieve.
547 For example, the pK_a values differ more than 11 pH units at the resting state between
548 the protonated SB and the Asp acids, the proton acceptors. That is to say, a
549 photoinduced reduction of one million times to the proton affinity of the SB must occur
550 simultaneously with an increase of one million times to the proton affinity of the
551 carboxylates. Even if these changes in proton affinity are achievable, there will be 10%
552 failed attempts of proton transfers at a prolonged equilibrium. The proton levee,
553 consisting of a few tyrosine residues, main chain carbonyls, and most importantly,
554 Arg82, is strategically constructed around the inner EC channel to prevent proton
555 backflow (Fig. 5). Their high pK_a values are not meant to be changed even though small
556 changes could be detected. In this study, the assumption of an affinity-driven proton
557 conductance is replaced by a mechanism of concentration-driven proton conductance
558 that is not necessarily synchronous to the early photocycles.
559
560 All chemical reactions involve energy transfer or conversion, known as enthalpy
561 change ΔH. This flow of energy in a unit time is the temporal rate of enthalpy change
562 dH/dt or power as a function of time. This function is usually far from a constant. The
563 peak power of a chemical reaction could be orders of magnitude greater than its
564 average power. This is particularly true for each individual molecular event compared
565 to a molecular ensemble. Consider the photochemical reaction of the retinal
566 isomerization in bR. Its peak power is reached at the U-turn of the SB (Figs. 2a and S2),
567 which accomplishes the initial deprotonation of each photocycle. The protein structure
568 of bR prevents a photochemical reaction from reaching its equilibrium as the
569 photoisomerization of the retinal switches the accessibility of the Schiff base to a
570 different reaction space. This is usually unachievable in chemical reactions of small
571 molecules.
572
573 **Acknowledgements**
574 This work is supported in part by the grant R01EY024363 from National Institutes of
575 Health. The following database and software are used in this work: CCP4 (ccp4.ac.uk),
576 Coot (www2.mrc-lmb.cam.ac.uk/Personal/pemsley/coot), dynamiX™ (Renz Research,

Inc.), gnuplot (gnuplot.info), PDB (rcsb.org), PHENIX (phenix-online.org), PyMOL (pymol.org), Python (python.org), and SciPy (scipy.org).

Competing interests

ZR is the founder of Renz Research, Inc. that currently holds the copyright of the computer software dynamiX™.

References

Adams, P.D., Afonine, P.V., Bunkóczi, G., Chen, V.B., Davis, I.W., Echols, N., Headd, J.J., Hung, L.-W., Kapral, G.J., Grosse-Kunstleve, R.W., et al. (2010). PHENIX: a comprehensive Python-based system for macromolecular structure solution. Acta Crystallogr. D Biol. Crystallogr. *D66*, 213–221.

Applebury, M.L., Peters, K.S., and Rentzepis, P.M. (1978). Primary intermediates in the photochemical cycle of bacteriorhodopsin. Biophys. J. *23*, 375–382.

Balashov, S.P., Govindjee, R., Kono, M., Imasheva, E., Lukashev, E., Ebrey, T.G., Crouch, R.K., Menick, D.R., and Feng, Y. (1993). Effect of the arginine-82 to alanine mutation in bacteriorhodopsin on dark adaptation, proton release, and the photochemical cycle. Biochemistry *32*, 10331–10343.

Balashov, S.P., Imasheva, E.S., Govindjee, R., and Ebrey, T.G. (1996). Titration of aspartate-85 in bacteriorhodopsin: what it says about chromophore isomerization and proton release. Biophys. J. *70*, 473–481.

Balashov, S.P., Imasheva, E.S., Ebrey, T.G., Chen, N., Menick, D.R., and Crouch, R.K. (1997). Glutamate-194 to cysteine mutation inhibits fast light-induced proton release in bacteriorhodopsin. Biochemistry *36*, 8671–8676.

van den Berg, R., Du-Jeon-Jang, Bitting, H.C., and El-Sayed, M.A. (1990). Subpicosecond resonance Raman spectra of the early intermediates in the photocycle of bacteriorhodopsin. Biophys. J. *58*, 135–141.

Braiman, M.S., Mogi, T., Marti, T., Stern, L.J., Khorana, H.G., and Rothschild, K.J. (1988). Vibrational spectroscopy of bacteriorhodopsin mutants: light-driven proton transport involves protonation changes of aspartic acid residues 85, 96, and 212. Biochemistry *27*, 8516–8520.

Braiman, M.S., Bousche, O., and Rothschild, K.J. (1991). Protein dynamics in the bacteriorhodopsin photocycle: submillisecond Fourier transform infrared spectra of the L, M, and N photointermediates. Proc. Natl. Acad. Sci. *88*, 2388–2392.

Brown, L.S., Bonet, L., Needleman, R., and Lanyi, J.K. (1993). Estimated acid dissociation constants of the Schiff base, Asp-85, and Arg-82 during the bacteriorhodopsin photocycle. Biophys. J. *65*, 124–130.

Chandonia, J.-M., and Brenner, S.E. (2006). The impact of structural genomics: expectations and outcomes. Science *311*, 347–351.

Dickopf, S., Alexiev, U., Krebs, M.P., Otto, H., Mollaaghababa, R., Khorana, H.G., and Heyn, M.P. (1995). Proton transport by a bacteriorhodopsin mutant, aspartic acid-85-->asparagine, initiated in the unprotonated Schiff base state. Proc. Natl. Acad. Sci. *92*, 11519–11523.

Druckmann, S., Ottolenghi, M., Pande, A., Pande, J., and Callender, R.H. (1982). Acid-base equilibrium of the Schiff base in bacteriorhodopsin. Biochemistry *21*, 4953–4959.

Ernst, O.P., Lodowski, D.T., Elstner, M., Hegemann, P., Brown, L.S., and Kandori, H. (2014). Microbial and animal rhodopsins: Structures, functions, and molecular mechanisms. Chem. Rev. *114*, 126–163.

Fahmy, K., Weidlich, O., Engelhard, M., Tittor, J., Oesterhelt, D., and Siebert, F. (1992). Identification of the proton acceptor of Schiff base deprotonation in bacteriorhodopsin: A Fourier-transform-infrared study of the mutant Asp85 → Glu in its natural lipid environment. Photochem. Photobiol. *56*, 1073–1083.

Fenno, L., Yizhar, O., and Deisseroth, K. (2011). The development and application of optogenetics. Annu. Rev. Neurosci. *34*, 389–412.

Friedrich, D., Brünig, F.N., Nieuwkoop, A.J., Netz, R.R., Hegemann, P., and Oschkinat, H. (2020). Collective exchange processes reveal an active site proton cage in bacteriorhodopsin. Commun. Biol. *3*, 4.

Garczarek, F., Wang, J., El-Sayed, M.A., and Gerwert, K. (2004). The Assignment of the Different Infrared Continuum Absorbance Changes Observed in the 3000–1800-cm−1 Region during the Bacteriorhodopsin Photocycle. Biophys. J. *87*, 2676–2682.

Garczarek, F., Brown, L.S., Lanyi, J.K., and Gerwert, K. (2005). Proton binding within a membrane protein by a protonated water cluster. Proc. Natl. Acad. Sci. *102*, 3633–3638.

Ge, X., and Gunner, M.R. (2016). Unraveling the mechanism of proton translocation in the extracellular half-channel of bacteriorhodopsin: Proton translocation in bacteriorhodopsin. Proteins Struct. Funct. Bioinforma. *84*, 639–654.

Gerwert, K., Hess, B., Soppa, J., and Oesterhelt, D. (1989). Role of aspartate-96 in proton translocation by bacteriorhodopsin. Proc. Natl. Acad. Sci. *86*, 4943–4947.

Gerwert, K., Souvignier, G., and Hess, B. (1990). Simultaneous monitoring of light-induced changes in protein side-group protonation, chromophore isomerization, and backbone motion of bacteriorhodopsin by time-resolved Fourier-transform infrared spectroscopy. Proc. Natl. Acad. Sci. *87*, 9774–9778.

Glynn, C., and Rodriguez, J.A. (2019). Data-driven challenges and opportunities in crystallography. Emerg. Top. Life Sci. ETLS20180177.

Govindjee, R., Balashov, S.P., and Ebrey, T.G. (1990). Quantum efficiency of the photochemical cycle of bacteriorhodopsin. Biophys. J. *58*, 597–608.

Govindjee, R., Misra, S., Balashov, S.P., Ebrey, T.G., Crouch, R.K., and Menick, D.R. (1996). Arginine-82 regulates the pKa of the group responsible for the light-driven proton release in bacteriorhodopsin. Biophys. J. *71*, 1011–1023.

Grigorieff, N., Ceska, T.A., Downing, K.H., Baldwin, J.M., and Henderson, R. (1996). Electron-crystallographic refinement of the structure of bacteriorhodopsin. J. Mol. Biol. *259*, 393–421.

Hackett, N.R., Stern, L.J., Chao, B.H., Kronis, K.A., and Khorana, H.G. (1987). Structure-function studies on bacteriorhodopsin. V. Effects of amino acid substitutions in the putative helix F. J. Biol. Chem. *262*, 9277–9284.

Henderson, R., and Unwin, P.N.T. (1975). Three-dimensional model of purple membrane obtained by electron microscopy. Nature *257*, 28–32.

Henderson, R., Baldwin, J.M., Ceska, T.A., Zemlin, F., Beckmann, E., and Downing, K.H. (1990). Model for the structure of bacteriorhodopsin based on high-resolution electron cryo-microscopy. J. Mol. Biol. *213*, 899–929.

Henry, E.R., and Hofrichter, J. (1992). Singular value decomposition: Application to analysis of experimental data. In Numerical Computer Methods, (Academic Press), pp. 129–192.

Jardetzky, O. (1966). Simple allosteric model for membrane pumps. Nature *211*, 969–970.

Jung, Y.O., Lee, J.H., Kim, J., Schmidt, M., Moffat, K., Šrajer, V., and Ihee, H. (2013). Volume-conserving trans–cis isomerization pathways in photoactive yellow protein visualized by picosecond X-ray crystallography. Nat. Chem. *5*, 212–220.

Kahan, A., Nahmias, O., Friedman, N., Sheves, M., and Ruhman, S. (2007). Following photoinduced dynamics in bacteriorhodopsin with 7-fs impulsive vibrational spectroscopy. J. Am. Chem. Soc. *129*, 537–546.

Kandori, H. (2015). Ion-pumping microbial rhodopsins. Front. Mol. Biosci. *2*.

Kobayashi, T., Saito, T., and Ohtani, H. (2001). Real-time spectroscopy of transition states in bacteriorhodopsin during retinal isomerization. Nature *414*, 531–534.

Kovacs, G.N., Colletier, J.-P., Grünbein, M.L., Yang, Y., Stensitzki, T., Batyuk, A., Carbajo, S., Doak, R.B., Ehrenberg, D., Foucar, L., et al. (2019). Three-dimensional view of ultrafast dynamics in photoexcited bacteriorhodopsin. Nat. Commun. *10*, 3177.

Lanyi, J.K., and Schobert, B. (2007). Structural changes in the L photointermediate of bacteriorhodopsin. J. Mol. Biol. *365*, 1379–1392.

Lewis, A., Spoonhower, J., Bogomolni, R.A., Lozier, R.H., and Stoeckenius, W. (1974). Tunable laser resonance Raman spectroscopy of bacteriorhodopsin. Proc. Natl. Acad. Sci. *71*, 4462–4466.

Li, Y.-T., Tian, Y., Tian, H., Tu, T., Gou, G.-Y., Wang, Q., Qiao, Y.-C., Yang, Y., and Ren, T.-L. (2018). A review on bacteriorhodopsin-based bioelectronic devices. Sensors *18*, 1368.

Liebschner, D., Afonine, P.V., Baker, M.L., Bunkóczi, G., Chen, V.B., Croll, T.I., Hintze, B., Hung, L.-W., Jain, S., McCoy, A.J., et al. (2019). Macromolecular structure determination using X-rays, neutrons and electrons: recent developments in Phenix. Acta Crystallogr. Sect. Struct. Biol. *75*, 861–877.

Lorenz-Fonfria, V.A., Saita, M., Lazarova, T., Schlesinger, R., and Heberle, J. (2017). pH-sensitive vibrational probe reveals a cytoplasmic protonated cluster in bacteriorhodopsin. Proc. Natl. Acad. Sci. *114*, E10909–E10918.

Lozier, R.H., Bogomolni, R.A., and Stoeckenius, W. (1975). Bacteriorhodopsin: a light-driven proton pump in Halobacterium Halobium. Biophys. J. *15*, 955–962.

Luecke, H., Schobert, B., Richter, H.-T., Cartailler, J.-P., and Lanyi, J.K. (1999a). Structure of bacteriorhodopsin at 1.55 Å resolution. J. Mol. Biol. *291*, 899–911.

Luecke, H., Schobert, B., Richter, H.-T., Cartailler, J.-P., and Lanyi, J.K. (1999b). Structural changes in bacteriorhodopsin during ion transport at 2 angstrom resolution. Science *286*, 255–260.

Luecke, H., Schobert, B., Cartailler, J.-P., Richter, H.-T., Rosengarth, A., Needleman, R., and Lanyi, J.K. (2000). Coupling photoisomerization of retinal to directional transport in bacteriorhodopsin. J. Mol. Biol. *300*, 1237–1255.

Marti, T., Otto, H., Mogi, T., Rösselet, S.J., Heyn, M.P., and Khorana, H.G. (1991). Bacteriorhodopsin mutants containing single substitutions of serine or threonine residues are all active in proton translocation. J. Biol. Chem. *266*, 6919–6927.

Marx, D., Tuckerman, M.E., Hutter, J., and Parrinello, M. (1999). The nature of the hydrated excess proton in water. Nature *397*, 601–604.

Mathias, G., and Marx, D. (2007). Structures and spectral signatures of protonated water networks in bacteriorhodopsin. Proc. Natl. Acad. Sci. *104*, 6980–6985.

McCarty, C.G. (1970). Chapter 9 syn-anti isomerizations and rearrangements. In The Chemistry of the Carbon-Nitrogen Double Bond, (John Wiley & Sons, Ltd), p. 363.

Moffat, K. (1989). Time-Resolved Macromolecular Crystallography. Annu. Rev. Biophys. Biophys. Chem. *18*, 309–332.

Moffat, K. (2001). Time-resolved biochemical crystallography: A mechanistic perspective. Chem Rev *101*, 1569–1582.

Mogi, T., Stern, L.J., Marti, T., Chao, B.H., and Khorana, H.G. (1988). Aspartic acid substitutions affect proton translocation by bacteriorhodopsin. Proc. Natl. Acad. Sci. *85*, 4148–4152.

Nango, E., Royant, A., Kubo, M., Nakane, T., Wickstrand, C., Kimura, T., Tanaka, T., Tono, K., Song, C., Tanaka, R., et al. (2016). A three-dimensional movie of structural changes in bacteriorhodopsin. Science *354*, 1552–1557.

Nogly, P., Weinert, T., James, D., Carbajo, S., Ozerov, D., Furrer, A., Gashi, D., Borin, V., Skopintsev, P., Jaeger, K., et al. (2018). Retinal isomerization in bacteriorhodopsin captured by a femtosecond x-ray laser. Science *361*, eaat0094.

Pebay-Peyroula, E., Rummel, G., Rosenbusch, J.P., and Landau, E.M. (1997). X-ray structure of bacteriorhodopsin at 2.5 Angstroms from microcrystals grown in lipidic cubic phases. Science *277*, 1676–1681.

Ren, Z. (2013a). Reaction trajectory revealed by a joint analysis of Protein Data Bank. PLoS ONE *8*, e77141.

Ren, Z. (2013b). Reverse engineering the cooperative machinery of human hemoglobin. PLoS ONE *8*, e77363.

Ren, Z. (2016). Molecular events during translocation and proofreading extracted from 200 static structures of DNA polymerase. Nucleic Acids Res. *6*, 1–13.

Ren, Z. (2019). Ultrafast structural changes decomposed from serial crystallographic data. J. Phys. Chem. Lett. *10*, 7148–7163.

Ren, Z. (2021). Photoinduced isomerization sampling of retinal in bacteriorhodopsin (bioRxiv doi:10.1101/2021.09.16.460656).

Ren, Z., Perman, B., Srajer, V., Teng, T.-Y., Pradervand, C., Bourgeois, D., Schotte, F., Ursby, T., Kort, R., Wulff, M., et al. (2001). A molecular movie at 1.8 Å resolution displays the photocycle of photoactive yellow protein, a eubacterial blue-light receptor, from nanoseconds to seconds. Biochemistry *40*, 13788–13801.

Ren, Z., Chan, P.W.Y., Moffat, K., Pai, E.F., Royer, W.E., Šrajer, V., and Yang, X. (2013). Resolution of structural heterogeneity in dynamic crystallography. Acta Cryst *D69*, 946–959.

Ren, Z., Ren, P.X., Balusu, R., and Yang, X. (2016). Transmembrane helices tilt, bend, slide, torque, and unwind between functional states of rhodopsin. Sci. Rep. *6*, 34129.

Ren, Z., Ayhan, M., Bandara, S., Bowatte, K., Kumarapperuma, I., Gunawardana, S., Shin, H., Wang, C., Zeng, X., and Yang, X. (2018). Crystal-on-crystal chips for in situ serial diffraction at room temperature. Lab. Chip *18*, 2246–2256.

Richter, H.T., Needleman, R., and Lanyi, J.K. (1996). Perturbed interaction between residues 85 and 204 in Tyr-185-->Phe and Asp-85-->Glu bacteriorhodopsins. Biophys. J. *71*, 3392–3398.

Royant, A., Edman, K., Ursby, T., Pebay-Peyroula, E., Landau, E.M., and Neutze, R. (2000). Helix deformation is coupled to vectorial proton transport in the photocycle of bacteriorhodopsin. Nature *406*, 645–648.

Sass, H.J., Büldt, G., Gessenich, R., Hehn, D., Neff, D., Schlesinger, R., Berendzen, J., and Ormos, P. (2000). Structural alterations for proton translocation in the M state of wild-type bacteriorhodopsin. Nature *406*, 649–653.

Schaffer, J.E., Kukshal, V., Miller, J.J., Kitainda, V., and Jez, J.M. (2021). Beyond X-rays: an overview of emerging structural biology methods. Emerg. Top. Life Sci. ETLS20200272.

Schmidt, M., Rajagopal, S., Ren, Z., and Moffat, K. (2003). Application of singular value decomposition to the analysis of time-resolved macromolecular X-ray data. Biophys. J. *84*, 2112–2129.

Schmidt, M., Graber, T., Henning, R., and Srajer, V. (2010). Five-dimensional crystallography. Acta Crystallogr. A *66*, 198–206.

Sheves, M., Albeck, A., Friedman, N., and Ottolenghi, M. (1986). Controlling the pKa of the bacteriorhodopsin Schiff base by use of artificial retinal analogues. Proc. Natl. Acad. Sci. *83*, 3262–3266.

Shin, H., Ren, Z., Zeng, X., Bandara, S., and Yang, X. (2019). Structural basis of molecular logic OR in a dual-sensor histidine kinase. Proc. Natl. Acad. Sci. *116*, 19973–19982.

Šrajer, V., Ren, Z., Teng, T.-Y., Schmidt, M., Ursby, T., Bourgeois, D., Pradervand, C., Schildkamp, W., Wulff, M., and Moffat, K. (2001). Protein conformational relaxation and ligand migration in myoglobin: A nanosecond to millisecond molecular movie from time-resolved Laue X-ray diffraction. Biochemistry *40*, 13802–13815.

Stoeckenius, W. (1999). Bacterial rhodopsins: Evolution of a mechanistic model for the ion pumps. Protein Sci. *8*, 447–459.

Stoeckenius, W., Lozier, R.H., and Bogomolni, R.A. (1979). Bacteriorhodopsin and the purple membrane of halobacteria. Biochim. Biophys. Acta BBA - Rev. Bioenerg. *505*, 215–278.

Takeda, K., Matsui, Y., Kamiya, N., Adachi, S., Okumura, H., and Kouyama, T. (2004). Crystal structure of the M intermediate of bacteriorhodopsin: Allosteric structural changes mediated by sliding movement of a transmembrane helix. J. Mol. Biol. *341*, 1023–1037.

Ursby, T., and Bourgeois, D. (1997). Improved estimation of structure-factor difference amplitudes from poorly accurate data. Acta Crystallogr. A *53*, 564–575.

Wang, J., and El-Sayed, M.A. (2001). Time-Resolved Fourier Transform Infrared Spectroscopy of the Polarizable Proton Continua and the Proton Pump Mechanism of Bacteriorhodopsin. Biophys. J. *80*, 961–971.

Weinert, T., Skopintsev, P., James, D., Dworkowski, F., Panepucci, E., Kekilli, D., Furrer, A., Brünle, S., Mous, S., Ozerov, D., et al. (2019). Proton uptake mechanism in bacteriorhodopsin captured by serial synchrotron crystallography. Science *365*, 61–65.

Wickstrand, C., Dods, R., Royant, A., and Neutze, R. (2015). Bacteriorhodopsin: Would the real structural intermediates please stand up? Biochim. Biophys. Acta *1850*, 536–553.

Yang, X., Ren, Z., Kuk, J., and Moffat, K. (2011). Temperature-scan cryocrystallography reveals reaction intermediates in bacteriophytochrome. Nature *479*, 428–432.

Zhong, Q., Ruhman, S., Ottolenghi, M., Sheves, M., Friedman, N., Atkinson, G.H., and Delaney, J.K. (1996). Reexamining the primary light-induced events in bacteriorhodopsin using a synthetic C13=C14-locked chromophore. J Am Chem Soc *118*, 12828–12829.

Zimanyi, L., Varo, G., Chang, M., Ni, B., Needleman, R., and Lanyi, J.K. (1992). Pathways of proton release in the bacteriorhodopsin photocycle. Biochemistry *31*, 8535–8543.

(2012). The Protein Data Bank at 40: Reflecting on the Past to Prepare for the Future. Structure *20*, 391–396.

Directional Proton Conductance in Bacteriorhodopsin Is Driven by Concentration Gradient, Not Affinity Gradient

Zhong Ren

Department of Chemistry, University of Illinois at Chicago, Chicago, IL 60607, USA
Renz Research, Inc., Westmont, IL 60559, USA

zren@uic.edu
ORCID 0000-0001-7098-3127

Figures and Legends

Ren: Concentration-driven proton conductance

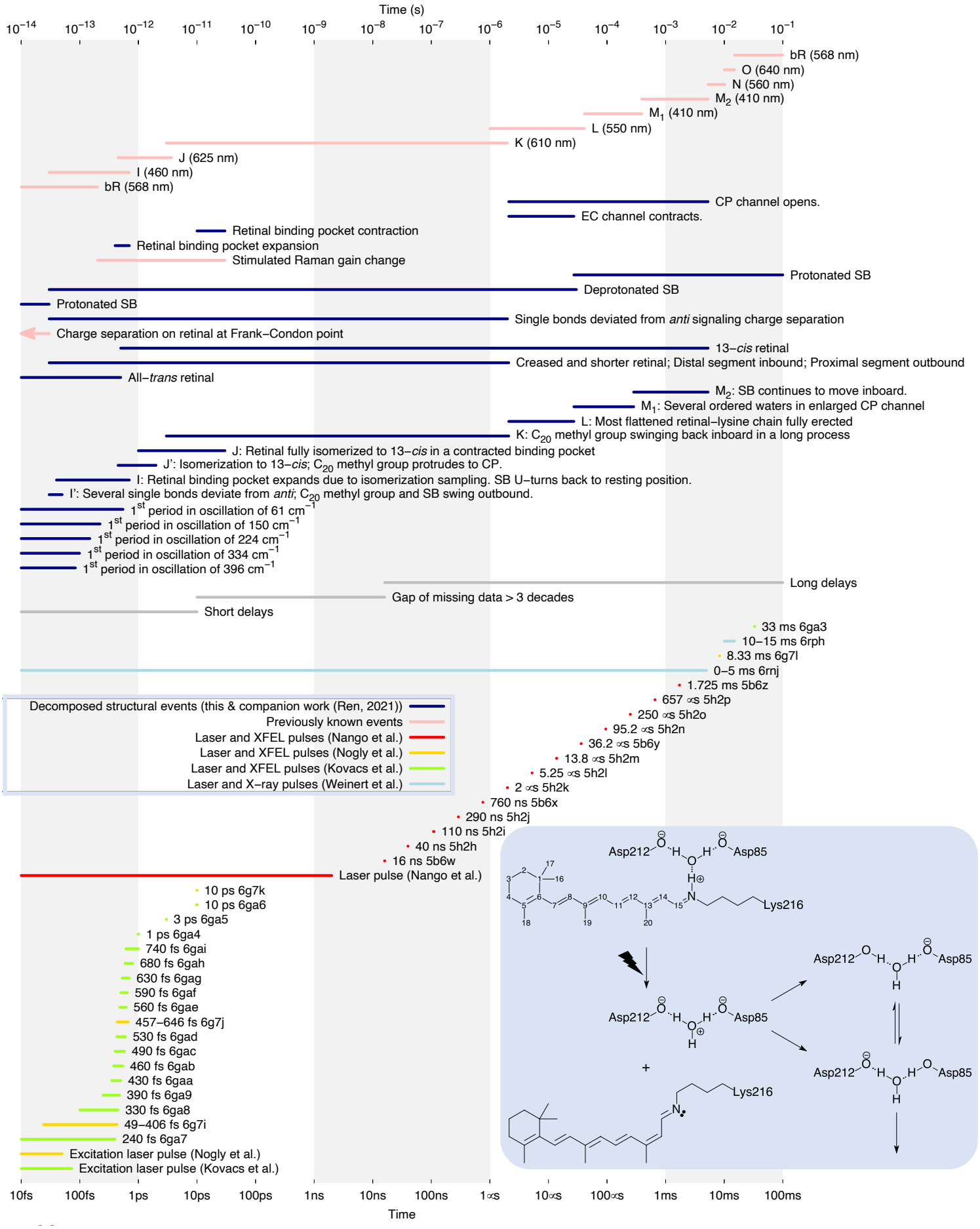

Figure 1. Gantt chart summarizing analyzed datasets and results. (Inset) Proposed scheme of deprotonation from SB. Deprotonation occurs at I′ around ~30 fs to form a transient hydronium ion (Fig. 2c). Another proton is transferred to either Asp85 or 212, between which an equilibrium is maintained over time. A second deprotonation in the next photocycle causes both Asp residues to be neutralized. One or more waters in the inner EC channel become overcharged with excess protons during the subsequent photocycles. A super-acidic inner EC channel then causes a second protonation of Arg82 to form a divalent guanidinium cation. The positive charged guanidinium group is attracted to the negative charged Glu residues in the outer EC channel and swings outward to form a salt bridge. The extra proton is discharged to the EC medium through the Glu residues and several waters in the outer EC channel, known as the proton release complex. The monovalent guanidinium returns for the next shuttling (Fig. 5).

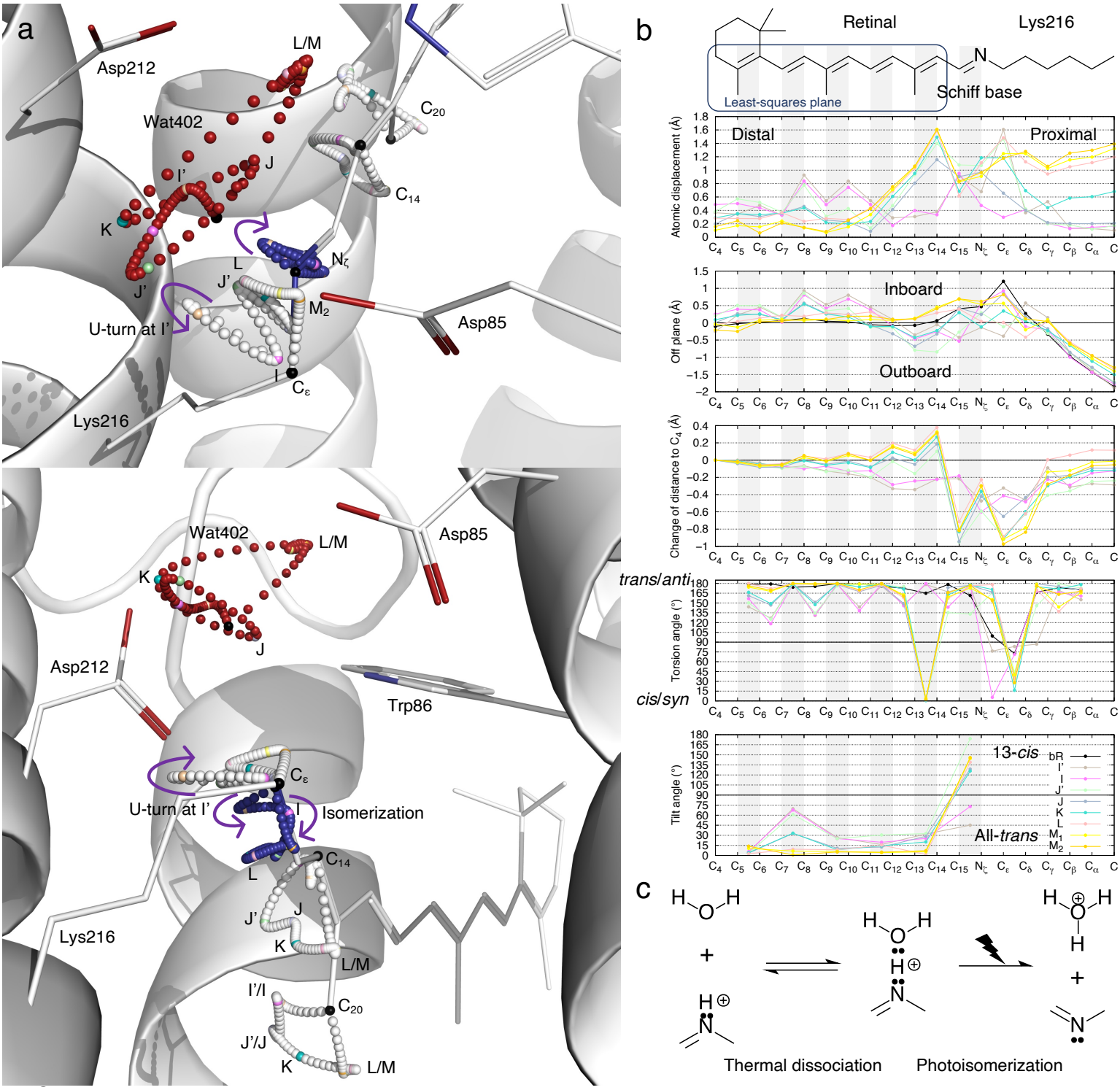

Figure 2. Trajectories of bacteriorhodopsin photocycle. (a) Two orthographical views of refined atomic trajectories. bR structure in the resting state is rendered in white ribbon and sticks. The photocycle trajectories of several atoms of the chromophore C_{14}, C_{20}, C_{ε},

N_ζ, and Wat402 are rendered as small spheres. Their positions in the ground state bR are in black. The intermediates I′, I, J′, J, K, L, M_1, and M_2 are colored differently. This color scheme (key in b) is consistently applied to all figures in this paper. Other small spheres along the atomic trajectories are in white for C, blue for N, and red for O. (b) Conformational parameters calculated from the refined chromophore. The chemical structure of the chromophore on top is aligned to the horizontal axis. Double bonds are shaded in gray. Atomic displacements of each intermediate from the resting state show greater changes in the proximal segment (top panel). A plane is least-squares fitted to C_4 through C_{14} of the resting state. This retinal plane is largely parallel to the three-fold axis of bR trimer. Therefore, one side of the plane where the three-fold axis is located is called inboard, and the opposite side of the plane away from the three-fold axis is called outboard (Ren, 2021). The distances of all atoms to this plane in the inboard and outboard directions show the curvature of the chromophore. The creased retinal in the early intermediates and the inboard protruding corner at C_ε in the resting state are clearly shown (2nd panel). Distances to atom C_4 are calculated for all refined chromophores. Changes in these distances with respect to the resting state show the shortened chromophore in I′ and I. Once isomerization to 13-*cis* occurs, the segment from C_{15} to C_δ around the SB becomes significantly closer to the β-ionone ring, while the distal segment of the retinal from C_{14} and beyond stretches (3rd panel). The torsion angles of single and double bonds quantify *anti*/*syn* or *trans*/*cis* for the ground state and all intermediates. Only a single bond can be twisted with its torsion angle near 90°. A double bond would spend very little time at a torsion angle near 90° compared to *trans* or *cis* configurations thus not easily observed (4th panel). Each double bond is least-squares fitted with a plane. The interplanar angle between one double bond and the corresponding one in the ground state measures the local tilting of the retinal (bottom panel). (c) Deprotonation from the Schiff base. In the resting state, a proton is situated between the SB N_ζ and the O of Wat402. Two lone pairs of electrons from N and O, respectively, are interacting with the proton. During thermal dissociation to the left, the proton stays with the SB with greater probability due to its greater proton affinity. This thermal process does not cause deprotonation from the SB, and it could revert. On the other hand, when the SB is abruptly displaced by the photoisomerization as observed here at ~30 fs (a), the proton inertia tips the balance of these two interactions. The proton cannot overcome its association with the water and accelerate fast enough with the SB. As a result, it stays with Wat402 to form a hydronium ion. This deprotonation

from the SB to the right is not governed by the proton affinities of two competing moieties based on chemical equilibrium. In addition, this process does not revert as the photoisomerization makes the SB no longer accessible from the EC half channel.

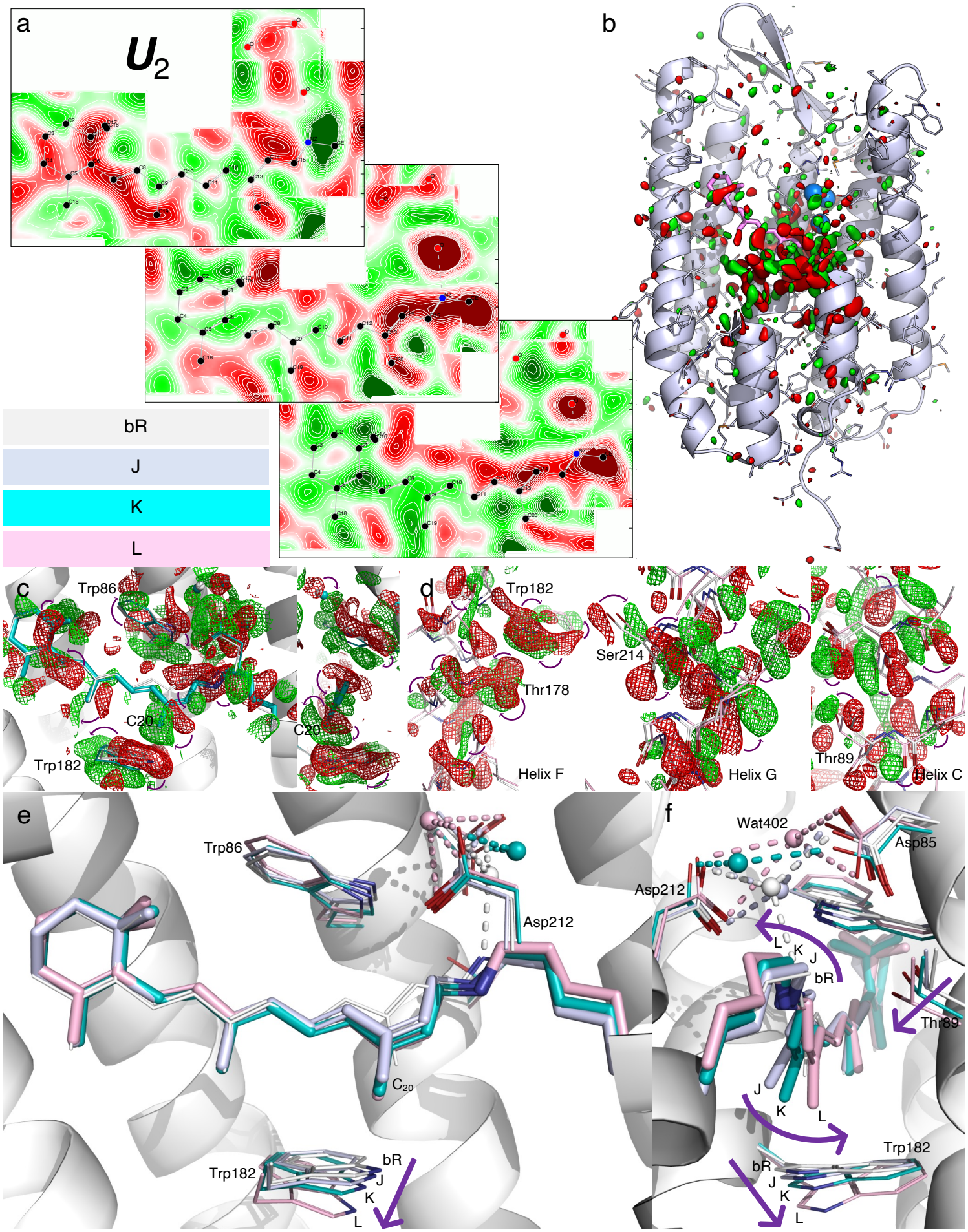
a
U_2
b
bR
J
K
L
c
Trp86
C20
Trp182
d
Trp182
Ser214
Thr178
Helix F
Helix G
Thr89
Helix C
e
Trp86
Asp212
C_{20}
Trp182
bR
J
K
L
f
Wat402
Asp85
Asp212
L
K
J
bR
Thr89
J
K
L
Trp182
bR
J
K
L

Figure 3. Intermediates J, K, and L. (a) Cross sections of component map $\boldsymbol{U}_2$ of the long delays > 10 ns. The middle cross section is an integration ±0.2 Å around the surface through the retinal. The top cross section is an integration 1.4-1.8 Å outboard from the retinal surface and the bottom is an integration 0.6-1 Å inboard. Green and red indicate electron density gain and loss, respectively. Stronger signals are around the proximal segment of the retinal, including Wat402. Positive and negative sheets of densities flank the distal segment of the retinal from inboard and outboard sides, respectively. This component is nearly constant in all long-delay difference maps with a dark dataset as reference (Fig. S4). (b) Overview of the component map $\boldsymbol{U}_2$ of the long delays contoured at $\pm 3\sigma$. The extraordinary signal-to-noise level is shown as the association with specific elements of the structure. Some parts of the structure are omitted to show the interior. (c) Two orthographical views of the reconstituted difference map K – bR from $\boldsymbol{U}_1$, $\boldsymbol{U}_2$, and $\boldsymbol{U}_3$ of the long delays (Fig. S5abc). The map is contoured at $\pm 2.5\sigma$ in green and red mesh, respectively. Atomic displacements are indicated by the arrows marking the negative and positive pairs of densities. (d) Reconstituted difference map L – bR from $\boldsymbol{U}_2$, $\boldsymbol{U}_3$, and $\boldsymbol{U}_6$ of the long delays (Fig. S5bcd). The map is contoured at $\pm 3.5\sigma$ in green and red mesh, respectively. The strongest signals are concentrated on the irregularities of helices F, G, and C (Fig. S10). (e and f) Two orthographical views of the refined retinal in J, K, and L compared with the resting state in white. The retinal is less creased in K and flattened in L compared to the previous intermediates (Fig. 2b 2nd panel). C_{20} methyl group is less and less tilted from its orientation in the resting state (Fig. 2b bottom panel). Wat402 with good electron density (Figs. S8 and S9) remains its H-bonds with both Asp85 and 212 in both K and L. Thr89 follows the motion of the SB toward outboard.

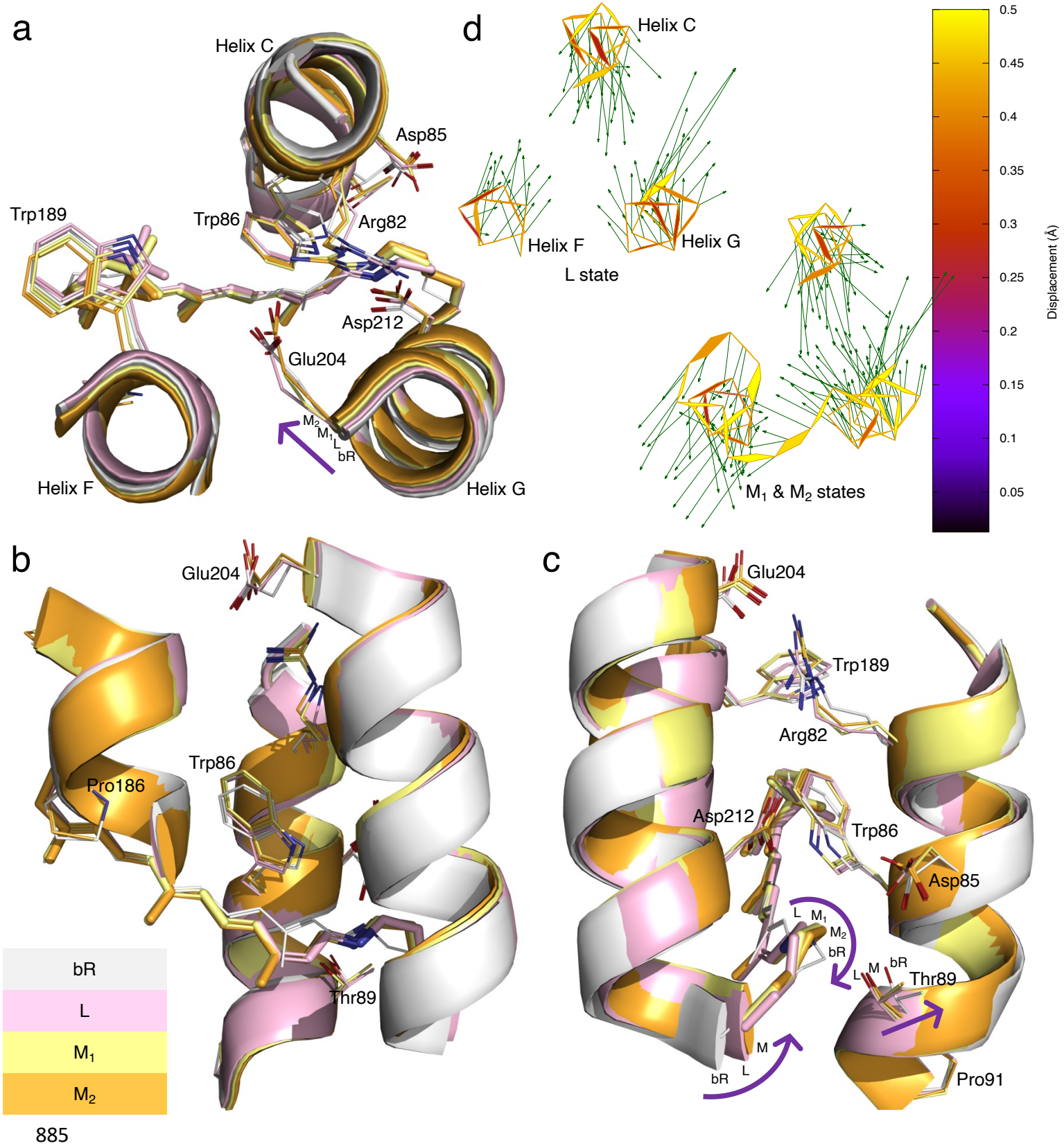
a
Helix C
Asp85
Trp189
Trp86
Arg82
Asp212
Glu204
M2
M1
L
bR
Helix F
Helix G
d
Helix C
Helix F
Helix G
L state
M1 & M2 states
0.5
0.45
0.4
0.35
0.3
0.25
0.2
0.15
0.1
0.05
Displacement (Å)
b
Glu204
Trp86
Pro186
Thr89
bR
L
M1
M2
885
c
Glu204
Trp189
Arg82
Asp212
Trp86
Asp85
L
M1
M2
bR
L
M
bR
Thr89
M
L
bR
Pro91

Figure 4. Intermediates L, M_1, and M_2. (a, b, and c) Three orthographical views of EC half channel. The refined structures of L, M_1, and M_2 in pink, yellow, and orange, respectively, are compared to the resting state in white. Several arrows mark the motions from the ground state bR to these intermediates or from these intermediates back to bR. The SB is moving more and more inboard since L and finally establishes the corner at C_ε protruding inboard in the ground state by isomerization back to all-*trans*. Meanwhile, Thr89 and helix C are pushed away. (d) Atomic displacements in the main chain around the EC half channel from the resting state to L and M are marked with arrows 10× as long as the actual displacements. The EC segments of helices C and G move closer to each other as Arg82 swings out. The same portion is displayed as in (a-c).

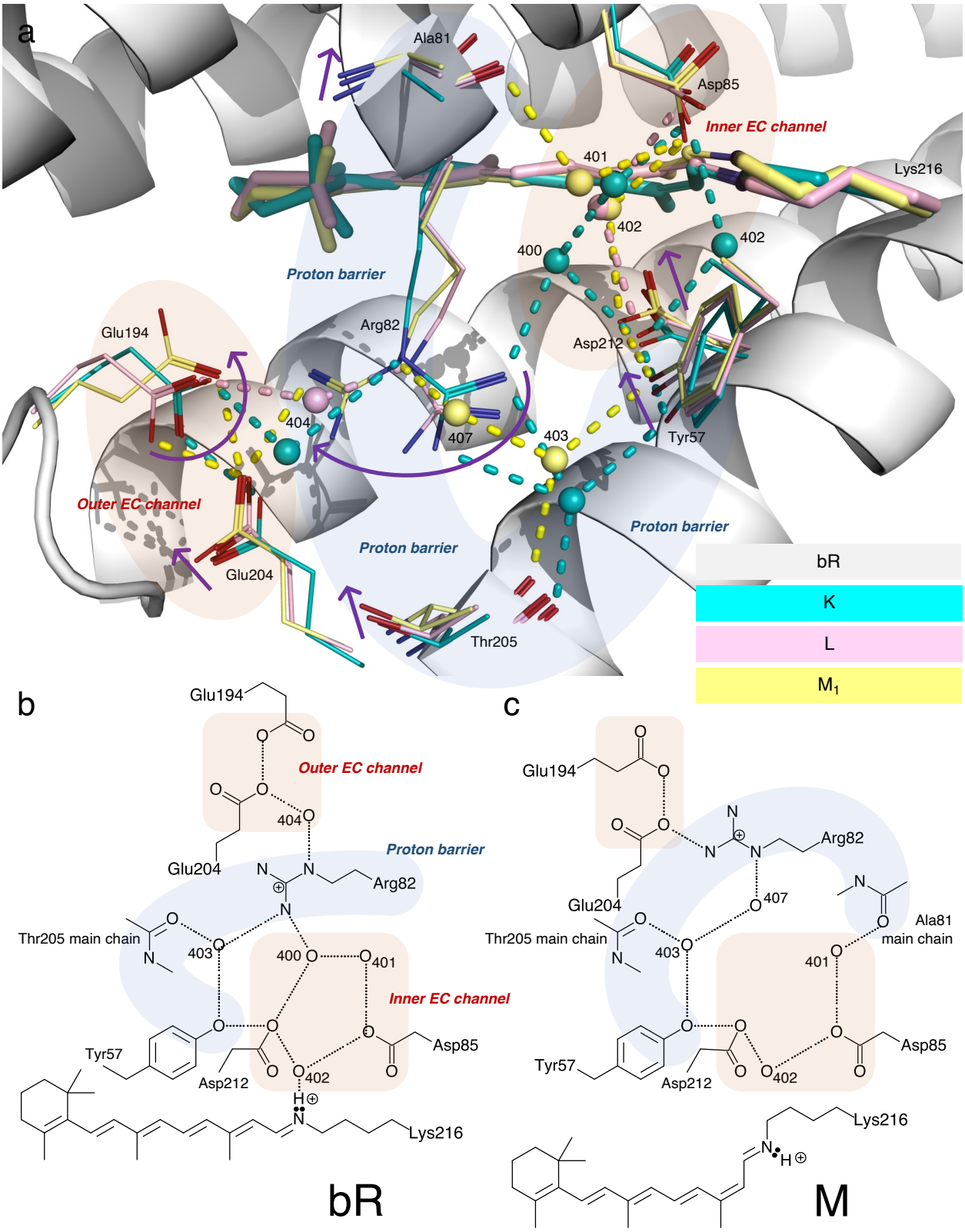
a
Ala81
Asp85
Inner EC channel
401
Lys216
402
400
402
Proton barrier
Glu194
Arg82
Asp212
404
407
403
Tyr57
Outer EC channel
Proton barrier
Proton barrier
Glu204
Thr205
bR
K
L
M1
b
Glu194
Outer EC channel
404
Proton barrier
Glu204
Arg82
Thr205 main chain
403
400
401
Inner EC channel
Tyr57
Asp85
Asp212
402
Lys216
bR
c
Glu194
Arg82
Glu204
407
Ala81
main chain
Thr205 main chain
403
401
Tyr57
Asp85
Asp212
402
Lys216
M

Figure 5. H-bond network in EC half channel. The EC half channel is decorated with acidic residues, such as Asp85 and 212 at the end, called inner EC channel shaded in red, and Glu9, 194, and 204 at the EC surface, called outer EC channel also shaded in red. Arg82, Tyr57, and 83 are located between these two layers that form a proton barrier shaded in blue (Fig. S1). (a) The refined structures of K in blue, L in pink, and M_1 in yellow are rendered in the framework of the resting state in white. Several arrows mark the motions of K → L → M_1. (b and c) The flattened networks in ground state and M state. Dashed lines mark H-bonds and salt bridges. Hydrogens, except the proton on the SB, are omitted due to the ambiguity in their associations with other atoms. 400 numbers are waters. The guanidinium group of Arg82 is already protonated with a positive charge at a neutral pH. The phenol hydroxyl groups of Tyr cannot be protonated anymore. These residues form a proton barrier shaded in blue between the inner aspartic acids and the outer glutamic acids shaded in red. The H-bond network in the EC half channel connects the inner acidic residues with the outer ones through the proton barrier of Arg82, Tyr57, and the main chain carbonyls of Ala81 and Thr205. Proton conductance through the proton barrier occurs only when excess protons are pumped into the inner EC channel, which becomes super-acidic. The guanidinium group of Arg82 is protonated for a second time under the extraordinary proton concentration.

Directional Proton Conductance in Bacteriorhodopsin Is Driven by Concentration Gradient, Not Affinity Gradient

Zhong Ren

Department of Chemistry, University of Illinois at Chicago, Chicago, IL 60607, USA
Renz Research, Inc., Westmont, IL 60559, USA

zren@uic.edu
ORCID 0000-0001-7098-3127

Supplementary Information

Intermediates K and L

Emerged from J around 10 ps, K lasts more than five decades into μs, which suggests that it is a struggle to achieve the next state L over a significant energy barrier. The creased retinal ever since I′ at the very first time point (Ren, 2021) is relaxing in K (blue; Figs. 3ef and S8). This slow and difficult relaxation could be driven in part by the energy stored in the creased 13-*cis* retinal and leads to global changes over the entire molecule. First, C_{20} methyl group is tilting less at 20° from its resting orientation (Fig. 2b bottom panel). Although protruded toward the CP direction due to the 13-*cis* configuration, the tilted C_{20} in J is not pointing to Trp182 directly (Fig. 3ef). Therefore, Trp182 is little affected in J. As C_{20} swings back in K, it starts to push Trp182 toward the CP and causes displacements in the main chain (Fig. 3cdef). The positive density that indicates the position of C_{20} in the reconstituted difference map K – bR forms an arc shape centered on the polyene chain (Fig. 3c). This observation strongly suggests that K is a process, rather than a discrete state, with C_{20} distributed along the arc leading toward the next state L, in which the methyl group is fully erected (Fig. 3ef). Second, the entire chromophore in K, except the most distal segment beyond C_8, is in a flat conformation with the double bond C_{13}=C_{14} in *cis* and the single bond C_ε–C_δ in *syn*. 12 consecutive torsion angles from C_8 to C_α deviate no more than 20° from *trans*/*cis* or *anti*/*syn*. The root-mean-squared deviation (rmsd) is 8.6° (Fig. 2b 4th panel). To achieve such energetically favorable conformation in the chromophore, the retinal anchor Lys216 is driven toward the EC direction, which causes a significant shift of the main chain in the vicinity. Third, again due to the 13-*cis* configuration, Trp86 on the EC side

moves with the proximal segment of the retinal toward the CP direction, which also causes movement in the main chain. All three developments above are the progresses in a long and hard work toward the goal to establish the state L with global consequences.

After five decades of time since tens of ps, the large energy barrier is finally overcome around several μs as described by the component map $\boldsymbol{U}_3$ (Fig. S5c) in the global transition of K → L. This transition is modeled here at a time constant of 2 μs (Fig. S7). The potential energy in the creased retinal established within tens of fs after photon absorption is spent to trigger this transition, at least in part. Other sources of potential energy, such as that stored in the bent helix C (Fig. S10a), could also drive the global transition. Strong signals in the reconstituted difference map L – bR (Fig. 3d) support the refined structure of L (pink; Fig. S9). The refined structure of L shows that the 13-*cis* retinal is finally flattened as its potential energy is consumed. 12 consecutive torsion angles from C_5 to C_δ, including the SB, deviate from *trans*/*cis* or *syn*/*anti* no more than 23° with an rmsd of 10° (Fig. 2b 4th panel). As a small cost, a couple of single bonds of Lys216 have to deviate from the perfect *syn* or *anti* conformation like those in the flat all-*trans* retinal in the resting state. The plane of the flattened 13-*cis* retinal has largely returned to the original plane of the all-*trans* retinal (Fig. 2b 2nd panel). C_{20} methyl group is pointing directly to Trp182, which causes helix F to displace (Figs. 3d and S10b). Leu93 in helix C is also affected by the protruding C_{20} methyl group back into the original retinal plane. On the other hand, the fully erected C_{20} displaces the anchor helix G with equally strong signals (Figs. 3d and S10c).

Intermediates M_1 and M_2

An increase of the component map $\boldsymbol{U}_1$ separating the long delays > 10 μs from the earlier ones is modeled as the L → M transition at a time constant of 27 μs. The M state could be split into two by an increase of the component map $\boldsymbol{U}_6$ at a time constant of 290 μs (Fig. S7). Signals in both $\boldsymbol{U}_1$ and $\boldsymbol{U}_6$ are distributed over the EC half of the molecule instead of globally (Fig. S5ad). Two similar structures M_1 and M_2 (yellow and orange) are refined according to the reconstituted difference maps M_1 – bR and M_2 – bR (Figs. S12 and S13). Since the L state, the SB is moving inboard mainly by twisting the torsion angle around N_ζ-C_ε (Fig. 2b 4th panel). C_ε in M_1 and M_2 has moved 0.6 and 0.8 Å, respectively, from its position in L. It seems that the conformation is approaching a

989 point poised to isomerize back to all-*trans*. In the meanwhile, Thr89 and helix C are
990 being pushed back toward inboard, which restores the kink of helix C in the resting
991 state (Fig. 4abc). The new development in the retinal displaces helix G further toward
992 the EC direction as previously observed (Takeda et al., 2004). On the other hand, the
993 stretched helix F in L springs back in M and becomes shorter than that in the resting
994 state. The EC segment of helix F turns around to move outboard since L (Fig. 4d).
995 However, the EC segments of helices C and G squeeze even tighter, while Arg82 swings
996 out of the way as observed previously (Luecke et al., 2000; Sass et al., 2000).
997
998 *Mutant functions*
999 Under the mechanism of proton conductance driven by concentration gradient
1000 presented here, a number of mutant functions are explained. How mutants behave, in
1001 return, further support these hypotheses. Proton pumping activity is abolished in
1002 D85N at neutral pH (Mogi et al., 1988). The remaining proton acceptor Asp212 is H-
1003 boned to the phenol hydroxy group of Tyr57 (Fig. S14). After two successful
1004 photocycles, Asp212 and Wat402 are both protonated. However, proton conductance is
1005 stopped at the carbonyl groups =O of both side chains of Asn85 and Asp212, the amide
1006 group -NH_2 of Asn85, and the hydroxy groups -OH of Tyr57 and 185, since none of
1007 them can be protonated further. The lack of a proton outlet causes the SB to be
1008 reprotonated quickly during I′ or I before isomerization. The proton pump stalls with
1009 repeated futile photocycles. It has been shown that the proton pumping activity of
1010 D85N can be somewhat restored at an alkaline pH (Dickopf et al., 1995), which is
1011 consistent with the concentration-driven proton conductance proposed here. The
1012 phenol hydroxy group of Tyr57, a weak acid, could start to conduct proton to Wat403
1013 and Arg82 only at an alkaline pH by deprotonation. On the other hand, some activity
1014 remains in D212N, which suggests a proton outlet going through Asp85, Wat401, 400,
1015 Arg82, and beyond (Fig. S14). In addition, Asp to Glu mutants are harder to assess
1016 because of their severe structural impacts. Proton pumping activity is also abolished in
1017 D212A (Mogi et al., 1988) perhaps due to a more mobile Wat402 or a hydronium that
1018 reprotonates the SB before isomerization or fails to withhold the proton during the SB
1019 U-turn. This mutant function further underscores the importance that Wat402 or a
1020 hydronium ion maintains its H-bonds to both Asp 85 and 212 throughout the
1021 photocycle as observed in this study despite its large traveling trajectory (Fig. 2a).
1022

1023 Mutants at the site of Arg82 are crucial tests to the mechanisms proposed here. M
1024 formation in the wildtype is pH-dependent at a few μs under alkaline pH and 85 μs at
1025 neutral pH (Balashov et al., 1993; Zimanyi et al., 1992), which nicely illustrates the
1026 concentration-gradient-driven proton conductance proposed here as faster proton
1027 release takes place driven by greater proton gradient. The proton barrier is breached in
1028 R82A mutant (Fig. 5). Therefore, the EC half channel must be filled with a continuous
1029 water network. Very little proton gradient can be established along the water filled
1030 channel during continuous pumping activity. R82A exhibits the same rate of proton
1031 uptake as the wildtype, but a rapid M formation without a pH dependency between
1032 neutral pH and pH10. Such rapid M formation is even faster than the wildtype under
1033 alkaline condition (Balashov et al., 1993). This is obviously due to the inability to
1034 establish the super-acidic inner EC channel without an intact proton barrier so that the
1035 protonation of Asp85 is accelerated compared to the wildtype. More interestingly, the
1036 fast phase of proton release is absent in R82A. Instead, a slow relaxation of 30 ms after
1037 proton uptake was observed (Balashov et al., 1993). Under the mechanism of a
1038 concentration-gradient-driven proton conductance, this slow relaxation is the
1039 spontaneous movement of the newly pumped proton in the same photocycle driven by
1040 a small gradient. Therefore, the "early release" in the fast phase of proton release
1041 cannot be observed without a well-established super-acidic inner EC channel in R82A.
1042 The "early release" observed from the wildtype is actually a much slower proton
1043 movement, in which a proton pumped into the super-acidic inner channel several
1044 photocycles ago is "squeezed out" by a newly pumped proton. This proton released
1045 from the wildtype appears to be coupled with or even faster than the protonation of
1046 Asp85.
1047
1048 Similar to R82A, another mutant R82Q also features rapid, biphasic formation of M
1049 at 1 and 160 μs but delayed proton release after uptake at neutral pH (Govindjee et al.,
1050 1996). However, unlike R82A, proton release from R82Q shows its strong pH-
1051 dependency. At neutral pH, the majority of proton release occurs late at 23 ms. If the
1052 pH increases to 8, most proton release precedes proton uptake at a few ms. The amide
1053 group on the side chain of the neutral residue Gln82 could be protonated by
1054 hydroniums in the inner EC channel. However, the amide group is not a sufficient
1055 proton barrier with its pK_a of -1.4 that could only establish a proton puddle less acidic
1056 compared to that of the wildtype. Another important factor to a smaller proton puddle

is that Gln is two bonds shorter than Arg. As a result, rapid proton release at a few ms is possible with a sufficient proton gradient under high pH. However, proton release is delayed to 23 ms as the proton gradient decreases under neutral pH. Again, the proton apparently released early is one of the protons accumulated in the inner EC channel, not the one freshly pumped in the same photocycle.

Supplementary Q&A

This study addresses four key questions regarding the operating mechanisms of the light-driven proton pump bR in addition to the question of isomerization sampling (Ren, 2021). Answers to these questions are somewhat scattered in the main text while evidence are presented to support these answers. Here the answers are recapped without the interruption of the technical details of the supporting data.

Q1) How does the protonated SB with a pK_a of 13.3 transfer its proton to the acidic acceptors and when?

A1) Which of the two weak interactions N_ζ:H^+:O402 survives an abrupt tare while the retinal prepares to undergo photoisomerization is determined by the inertia of the proton (Fig. 2c). It is decisive that the proton dissociates from the SB due to its inertia at the beginning of the retinal photoisomerization. The SB nitrogen makes a rapid U-turn at ~30 fs (Figs. 2a and S2). A force > 500 pN is required to accelerate the proton as fast as the SB. Breaking the H-bond H_2O402:H^+ is nearly as costly as breaking the association N_ζ:H^+ (Figs. 1 inset and 2c). Therefore, the proton joins Wat402 to form a hydronium ion due to its inertia instead of keeping up to maintain the SB protonated. Such a proton transfer uphill over 15 pH units within tens of fs is not achieved by a chemical equilibrium, thus not governed by pK_a values. This proton transfer requires a high peak power dH/dt localized at the SB. On the other hand, holding Wat402 in place by both Asp85 and 212 symmetrically from inboard and outboard is as important as the ultrafast shaking of the SB. This proton transfer uses the same mechanism of the tablecloth trick. The early deprotonation from the SB is a separate event from the protonation of Asp85 ten decades later at the formation of M state. Vibrational signatures from the neutralization of the carboxylates previously observed do not imply SB deprotonation. This light-driven reaction of a proton pump differs markedly from a thermal driven chemical equilibrium (Fig. 2c).

Q2) Which molecular event, the isomerization, or another event, switches the accessibility of the SB from EC side to CP side and how does the SB avoid reprotonation on the wrong side?

A2) Immediately before isomerization in the I state, the SB is reoriented toward the inboard while Wat402, a hydronium at this moment, is displaced to the outboard. This geometry is very bad for proton exchange (Fig. S3). Therefore, the accessibility of the SB is already limited even before isomerization. However, accessibility switch of the SB is finally accomplished by the photoisomerization during I → J′. The photoisomerization must be quick enough to prevent a chemical equilibrium in the EC half channel. If the equilibrium is reached before isomerization, the SB is reprotonated from the EC side, and the quantum yield of the proton pump is sacrificed (Govindjee et al., 1990).

Q3) How are protons conducted > 15 Å through the rollercoasting pK_a values and released into the EC medium from the SB of a high pK_a through aspartic acids of low pK_a, arginine (strictly speaking, its guanidinium ion) and tyrosine of high pK_a, and glutamic acids of low pK_a again?

A3) The EC half channel is obviously not lined with residues of pK_a values in a monotonic order (Figs. 5 and S1). Despite numerous observations of pK_a changes, no sufficient evidence supports photoinduced changes to form an ascending order of pK_a values either. Proton is therefore not conducted along an ascending order of pK_a values driven by the proton affinity (Stoeckenius, 1999; Stoeckenius et al., 1979). Instead, proton conductance is driven by concentration gradient, not by affinity gradient. The guanidinium ion of the arginine and tyrosines of high pK_a, together with several main chain carbonyls, are arranged to function as a proton levee so that protons could only overflow outward from a super-acidic inner EC channel established after several successful cycles of proton pumping. No proton is released during the first a few cycles of productive pumping until a sufficient proton gradient is established. Under a super-acidic condition in the inner EC channel, the guanidinium group of Arg82 is protonated for a second time to form a divalent cation. While it swings outward, the extra proton is discharged to Glu194, 204, and a water cluster in the outer EC channel, the proton

release complex. Protons could never flow backward into the cell as long as sufficient water is available in the EC medium. The rollercoasting pK_a values ensure the concentration-driven outward conductance of protons and prevent the concentration-driven inward conductance during dark, that is, a unidirectional valve.

Q4) How is a gradient-driven proton leak prevented in the resting state and during the pumping motions?

A4) A potential proton leak back into the cell during dark is prevented by the exact mechanism that conducts proton outward (A3). However, the chance of proton leak increases dramatically during the molecular motions of proton pumping because the inner EC channel becomes super acidic and the retinal and its surrounding are in constant motions. Lys216 forms a corner at C_ε that protrudes inboard and makes a van der Waals contact with Thr89 in helix C (Figs. 2b and S10a). Pressed by the corner at C_ε, helix C is kinked and bends away. This contact is a seal between two half channels. This seal could be broken briefly in I′ state but inconsequential. C_δ-C_ε moves outboard in L state once again due to a flattened 13-*cis* retinal (Figs. 2b and S10a). But this motion is slow enough to allow the spring-loaded helix C to react. Helix C straightens and maintains the contact between the chromophore and Thr89 to prevent a concentration-gradient-driven proton leak back into the CP (Figs. 3f and 4c). During the M states, the corner at C_ε is reestablished. It pushes Thr89 and helix C to restore its kink.

Methods

From the outset, the key presumption is that every crystallographic dataset, at a given temperature and a given time delay after the triggering of the photochemical reaction, captures a mixture of unknown number of intermediate species at unknown fractions. Needless to say, all structures of the intermediates are also unknown except the structure at the ground state that has been determined and well refined by static crystallography. A simultaneous solution of all these unknowns requires multiple datasets that are collected at various temperatures or time delays so that a common set of intermediate structures are present in these datasets with variable ratios. If the number of available datasets is far greater than the number of unknowns, a linear system can be established to overdetermine the unknowns with the necessary stereochemical restraints (Ren et al., 2013). This analytical strategy is recapped below.

The methodological advance in this work and the companion work (Ren, 2021) is the refinement of each pure intermediate structure that has been deconvoluted from multiple mixtures. Structure factor amplitudes of a single conformation free of heterogeneity are overdetermined. Unlike the conventional crystallography, such a deconvoluted dataset of structure factor amplitudes are not observed directly from any crystal but computed from many experimental datasets. It could be considered as an extrapolated dataset "on steroids" if compared to the traditional extrapolation of small differences, such as, 3Fo-2Fc map, a technique often used to overcome a partial occupancy of an intermediate structure, except that this deconvolution method is an interpolation among many experimental datasets rather than an extrapolation. The standard structural refinement software is taken full advantage of with the built-in stereochemical constraints, e.g. PHENIX (Adams et al., 2010; Liebschner et al., 2019). In case that the computed deconvolution has not achieved a single pure structural species, the structural refinement is expected to make such indication.

Difference Fourier maps

A difference Fourier map is synthesized from a Fourier coefficient set of F_{light}-$F_{\text{reference}}$ with the best available phase set, often from the ground state structure. Before Fourier synthesis, F_{light} and $F_{\text{reference}}$ must be properly scaled to the same level so that the distribution of difference values is centered at zero and not skewed either way. A weighting scheme proven effective assumes that a greater amplitude of a difference Fourier coefficient F_{light}-$F_{\text{reference}}$ is more likely caused by noise than by signal (Ren et al., 2001, 2013; Šrajer et al., 2001; Ursby and Bourgeois, 1997). Both the dark and light datasets can serve as a reference in difference maps. If a light dataset at a certain delay is chosen as a reference, the difference map shows the changes since that delay time but not the changes prior to that delay. However, both the dark and light datasets must be collected in the same experiment. A cross reference from a different experimental setting usually causes large systematic errors in the difference map that would swamp the desired signals. Each difference map is masked 3.5 Å around the entire molecule of bacteriorhodopsin (bR). No lipid density is analyzed.

Meta-analysis of protein structures

Structural meta-analysis based on singular value decomposition (SVD) has been conducted in two forms. In one of them, an interatomic distance matrix is calculated from each protein structure in a related collection. SVD of a data matrix consists of these distance matrices enables a large-scale joint structural comparison but requires no structural alignment (Ren, 2013a, 2013b, 2016). In the second form, SVD is performed on a data matrix of electron density maps of related protein structures (Ren, 2019; Ren et al., 2013; Schmidt et al., 2003, 2010). Both difference electron density maps that require a reference dataset from an isomorphous crystal and simulated annealing omit maps that do not require the same unit cell and space group of the crystals are possible choices in a structural meta-analysis (Ren, 2019; Ren et al., 2013). The distance matrices or the electron density maps that SVD is performed on are called core data. Each distance matrix or electron density map is associated with some metadata that describe the experimental conditions under which the core data are obtained, such as temperature, pH, light illumination, time delay, mutation, etc. These metadata do not enter the SVD procedure. However, they play important role in the subsequent interpretation of the SVD result. This computational method of structural analysis takes advantage of a mathematical, yet practical, definition of conformational space with limited dimensionality (Ren, 2013a). Each experimentally determined structure is a snapshot of the protein structure. A large number of such snapshots taken under a variety of experimental conditions, the metadata, would collectively provide a survey of the accessible conformational space of the protein structure and reveal its rection trajectory. Such joint analytical strategy would not be effective in early years when far fewer protein structures were determined to atomic resolution. Recent rapid growth in protein crystallography, such as in structural genomics (Chandonia and Brenner, 2006, 2012) and in serial crystallography (Glynn and Rodriguez, 2019; Schaffer et al., 2021), has supplied the necessarily wide sampling of protein structures for a joint analytical strategy to come of age. The vacancies or gaps in a conformational space between well-populated conformational clusters often correspond to less stable transient states whose conformations are difficult to capture, if not impossible. These conformations are often key to mechanistic understanding and could be explored by a back calculation based on molecular distance geometry (Ren, 2013a, 2016), the chief computational algorithm in nucleic magnetic resonance spectroscopy (NMR), and by a structure refinement based on reconstituted dataset, a major methodological advance in this work (see below).

These structures refined to atomic resolution against reconstituted datasets may reveal short-lived intermediate conformation hard to be captured experimentally. Unfortunately, a protein structure refined against a reconstituted dataset currently cannot be recognized by the Protein Data Bank (PDB). Because crystallographic refinement of a macromolecular structure is narrowly defined as a correspondence from one dataset to one structure. A never-observed dataset reconstituted from a collection of experimental datasets does not match the well-established crystallographic template of PDB; let alone a refinement of crystal structure with the NMR algorithm.

A distance matrix contains M pairwise interatomic distances of a structure in the form of Cartesian coordinates of all observed atoms. An everyday example of distance matrix is an intercity mileage chart appended to the road atlas. Differences in the molecular orientation, choice of origin, and crystal lattice among all experimentally determined structures have no contribution to the distance matrices. Due to its symmetry, only the lower triangle is necessary. A far more intimate examination of protein structures in PDB is a direct analysis of their electron density maps instead of the atomic coordinates. M such (difference) electron densities, often called voxels in computer graphics, are selected by a mask of interest. In the case of difference maps, only the best refined protein structure in the entire collection supplies a phase set for Fourier synthesis of electron density maps. This best structure is often the ground state structure determined by static crystallography. Other refined atomic coordinates from the PDB entries are not considered in the meta-analysis. That is to say, a meta-analysis of difference electron density maps starts from the X-ray diffraction data archived in PDB rather than the atomic coordinates interpreted from the diffraction data, which removes any potential model bias.

Singular value decomposition of (difference) electron density maps

An electron density map, particularly a difference map as emphasized here, consists of density values on an array of grid points within a mask of interest. All M grid points in a three-dimensional map can be serialized into a one-dimensional sequence of density values according to a specific protocol. It is not important what the protocol is as long as a consistent protocol is used to serialize all maps of the same grid setting and size, and a reverse protocol is available to erect a three-dimensional map from a sequence of M densities. Therefore, a set of N serialized maps, also known as vectors in linear

algebra, can fill the columns of a data matrix **A** with no specific order, so that the width of **A** is N columns, and the length is M rows. Often, $M >> N$, thus **A** is an elongated matrix. If a consistent protocol of serialization is used, the corresponding voxel in all N maps occupies a single row of matrix **A**. This strict correspondence in a row of matrix **A** is important. Changes of the density values in a row from one structure to another are due to either signals, systematic errors, or noises. Although the order of columns in matrix **A** is unimportant, needless to say, the metadata associated with each column must remain in good bookkeeping.

SVD of the data matrix **A** results in $\mathbf{A} = \mathbf{UWV}^{\mathrm{T}}$, also known as matrix factorization. Matrix **U** has the same shape as **A**, that is, N columns and M rows. The N columns contain decomposed basis components $\boldsymbol{U}_k$, known as left singular vectors of M items, where $k = 1, 2, \ldots, N$. Therefore, each component $\boldsymbol{U}_k$ can be erected using the reverse protocol to form a three-dimensional map. This decomposed elemental map can be presented in the same way as the original maps, for example, rendered in molecular graphics software such as Coot and PyMol. It is worth noting that these decomposed elemental maps or map components $\boldsymbol{U}_k$ are independent of any metadata. That is to say, these components remain constant when the metadata vary. Since each left singular vector $\boldsymbol{U}_k$ has a unit length due to the orthonormal property of SVD (see below), that is, $|\boldsymbol{U}_k| = 1$, the root mean squares (rms) of the items in a left singular vector is $1/\sqrt{M}$ that measures the quadratic mean of the items.

The second matrix **W** is a square matrix that contains all zeros except for N positive values on its major diagonal, known as singular values w_k. The magnitude of w_k is considered as a weight or significance of its corresponding component $\boldsymbol{U}_k$. The third matrix **V** is also a square matrix of $N \times N$. Each column of **V** or row of its transpose $\mathbf{V}^{\mathrm{T}}$, known as a right singular vector $\boldsymbol{V}_k$, contains the relative compositions of $\boldsymbol{U}_k$ in each of the N original maps. Therefore, each right singular vector $\boldsymbol{V}_k$ can be considered as a function of the metadata. Right singular vectors also have the same unit length, that is, $|\boldsymbol{V}_k| = 1$. Effectively, SVD separates the constant components independent of the metadata from the compositions that depend on the metadata.

A singular triplet denotes 1) a decomposed component $\boldsymbol{U}_k$, 2) its singular value w_k, and 3) the composition function $\boldsymbol{V}_k$. Singular triplets are often sorted in a descending

order of their singular values w_k. Only a small number of n significant singular triplets identified by the greatest singular values w_1 through w_n can be used in a linear combination to reconstitute a set of composite maps that closely resemble the original ones in matrix **A**, where $n < N$. For example, the original map in the ith column of matrix **A** under a certain experimental condition can be closely represented by the ith composite map $w_1v_{1i}\boldsymbol{U}_1 + w_2v_{2i}\boldsymbol{U}_2 + \ldots + w_nv_{ni}\boldsymbol{U}_n$, where $(v_{1i}, v_{2i}, \ldots)$ is from the ith row of matrix **V**. The coefficient set for the linear combination is redefined here as $c_{ki} = w_kv_{ki}/\sqrt{M}$. The rms of the values in a map component, or the average magnitude measured by the quadratic mean, acts as a constant scale factor that resets the modified coefficients c_{ki} back to the original scale of the core data, such as Å for distance matrices and e^-/Å^3 for electron density maps if these units are used in the original matrix **A**. Practically, an electron density value usually carries an arbitrary unit without a calibration, which makes this scale factor unnecessary. In the linear combination $c_{1i}\boldsymbol{U}_1 + c_{2i}\boldsymbol{U}_2 + \ldots + c_{ni}\boldsymbol{U}_n$, each component $\boldsymbol{U}_k$ is independent of the metadata while how much of each component is required for the approximation, that is, c_{ki}, depends on the metadata.

Excluding the components after $\boldsymbol{U}_n$ in this approximation is based on an assumption that the singular values after w_n are very small relative to those from w_1 through w_n. As a result, the structural information evenly distributed in all N original maps is effectively concentrated into a far fewer number of n significant components, known as information concentration or dimension reduction. On the other hand, the trailing components in matrix **U** contain inconsistent fluctuations and random noises. Excluding these components effectively rejects noises (Schmidt et al., 2003). The least-squares property of SVD guarantees that the rejected trailing components sums up to the least squares of the discrepancies between the original core data and the approximation using the accepted components.

However, no clear boundary is guaranteed between signals, systematic errors, and noises. Systematic errors could be more significant than the desired signals. Therefore, excluding some components from 1 through n is also possible. If systematic errors are correctly identified, the reconstituted map without these significant components would no longer carry the systematic errors.

The orthonormal property of SVD

The solution set of SVD must guarantee that the columns in **U** and **V**, the left and right singular vectors $\boldsymbol{U}_k$ and $\boldsymbol{V}_k$, are orthonormal, that is, $\boldsymbol{U}_h \bullet \boldsymbol{U}_k = \boldsymbol{V}_h \bullet \boldsymbol{V}_k = 0$ (ortho) and $\boldsymbol{U}_k \bullet \boldsymbol{U}_k = \boldsymbol{V}_k \bullet \boldsymbol{V}_k = 1$ (normal), where $h \neq k$ but both are from 1 to N. The orthonormal property also holds for the row vectors. As a result, each component $\boldsymbol{U}_k$ is independent of the other components. In other words, a component cannot be represented by a linear combination of any other components. However, two physical or chemical parameters in the metadata, such as temperature and pH, may cause different changes to a structure. These changes are not necessarily orthogonal. They could exhibit some correlation. Therefore, the decomposed components $\boldsymbol{U}_k$ not necessarily represent any physically or chemically meaningful changes (see below).

Due to the orthonormal property of SVD, an N-dimensional Euclidean space is established, and the first n dimensions define its most significant subspace. Each coefficient set $\boldsymbol{c}_i = (c_{1i}, c_{2i}, \ldots, c_{ni})$ of the ith composite map is located in this n-dimensional subspace. All coefficient sets for $i = 1, 2, \ldots, N$ in different linear combinations to approximate the N original maps in a least-squares sense can be represented by N points or vectors $\boldsymbol{c}_1, \boldsymbol{c}_2, \ldots, \boldsymbol{c}_N$ in the Euclidean subspace. This n-dimensional subspace is essentially the conformational space as surveyed by the jointly analyzed core data. The conformational space is presented as scatter plots with each captured structure represented as a dot located at a position determined by the coefficient set $\boldsymbol{c}_i$ of the ith observed map. When the subspace has greater dimensionality than two, multiple two-dimensional orthographical projections of the subspace are presented. These scatter plots are highly informative to reveal the relationship between the (difference) electron density maps and their metadata.

If two coefficient sets $\boldsymbol{c}_i \approx \boldsymbol{c}_j$, they are located close to each other in the conformational space. Therefore, these two structures i and j share two similar conformations. Two structures located far apart from each other in the conformational space are distinct in their conformations, and distinct in the compositions of the map components. A reaction trajectory emerges in this conformational space if the temporal order of the core data is experimentally determined (Figs. S4 and S7). Otherwise, an order could be assigned to these structures based on an assumed smoothness of conformational changes along a reaction trajectory (Ren, 2013a, 2013b, 2016). Causation

and consequence of structural motions could be revealed from the order of the structures in a series, which may further lead to structural mechanism. In addition, an off-trajectory location in the conformational space or a location between two clusters of observed structures represents a structure in a unique conformation that has never been experimentally captured. Such a hypothetical structure can be refined against a reconstituted distance matrix using molecular distance geometry (Ren, 2013a, 2013b, 2016) or a reconstituted electron density map with the method proposed below.

Rotation in SVD space

Dimension reduction is indeed effective in meta-analysis of protein structures when many datasets are evaluated at the same time. However, the default solution set of SVD carries complicated physical and chemical meanings that are not immediately obvious. The interpretation of a basis component $\boldsymbol{U}_k$, that is, "what-does-it-mean", requires a clear demonstration of the relationship between the core data and their metadata. The outcome of SVD does not guarantee any physical meaning in a basis component. Therefore, SVD alone provides no direct answer to "what-does-it-mean", thus its usefulness is very limited to merely a mathematical construction. However, the factorized set of matrices **U**, **W**, and **V** from SVD is not a unique solution. That is to say, they are not the only solution to factorize matrix **A**. Therefore, it is very important to find one or more alternative solution sets that are physically meaningful to elucidate a structural interpretation. The concept of a rotation after SVD was introduced by Henry & Hofrichter (Henry and Hofrichter, 1992). But they suggested a protocol that fails to preserve the orthonormal and least-squares properties of SVD. The rotation protocol suggested by Ren incorporates the metadata into the analysis and combines with SVD of the core data. This rotation achieves a numerical deconvolution of multiple physical and chemical factors after a pure mathematical decomposition, and therefore, provides a route to answer the question of "what-does-it-mean" (Ren, 2019). This rotation shall not be confused with a rotation in the three-dimensional real space, in which a molecular structure resides.

A rotation in the n-dimensional Euclidean subspace is necessary to change the perspective before a clear relationship emerges to elucidate scientific findings. It is shown below that two linear combinations are identical before and after a rotation

applied to both the basis components and their coefficients in a two-dimensional subspace of h and k. That is,

$$c_h\boldsymbol{U}_h + c_k\boldsymbol{U}_k = f_h\boldsymbol{R}_h + f_k\boldsymbol{R}_k, \tag{1}$$

where c_h and c_k are the coefficients of the basis components $\boldsymbol{U}_h$ and $\boldsymbol{U}_k$ before the rotation; and f_h and f_k are the coefficients of the rotated basis components $\boldsymbol{R}_h$ and $\boldsymbol{R}_k$, respectively. The same Givens rotation of an angle θ is applied to both the components and their coefficients:

$$\begin{cases} \boldsymbol{R}_h = \boldsymbol{U}_h\cos\theta - \boldsymbol{U}_k\sin\theta; \\ \boldsymbol{R}_k = \boldsymbol{U}_h\sin\theta + \boldsymbol{U}_k\cos\theta. \end{cases} \tag{2}$$

Obviously, the rotated components $\boldsymbol{R}_h$ and $\boldsymbol{R}_k$ remain mutually orthonormal and orthonormal to other components. And

$$\begin{cases} f_h = s_h t_h = c_h\cos\theta - c_k\sin\theta; \\ f_k = s_k t_k = c_h\sin\theta + c_k\cos\theta. \end{cases} \tag{3}$$

Here $s_{h|k} = \sqrt{\sum f_{h|k}^2}$ are the singular values that replace w_h and w_k, respectively, after the rotation. They may increase or decrease compared to the original singular values so that the descending order of the singular values no longer holds. $\boldsymbol{T}_{h|k} = (t_{h|k1}, t_{h|k2}, \ldots, t_{h|kN}) = (f_{h|k1}, f_{h|k2}, \ldots, f_{h|kN})/s_{h|k}$ are the right singular vectors that replace $\boldsymbol{V}_h$ and $\boldsymbol{V}_k$, respectively. $\boldsymbol{T}_h$ and $\boldsymbol{T}_k$ remain mutually orthonormal after the rotation and orthonormal to other right singular vectors that are not involved in the rotation.

Eq. 1 holds because the dot product of two vectors does not change after both vectors rotate the same angle. To prove Eq. 1 in more detail, Eqs. 2 and 3 are combined and expanded. All cross terms of sine and cosine are self-canceled:

$$\begin{aligned} f_h\boldsymbol{R}_h + f_k\boldsymbol{R}_k &= (c_h\cos\theta - c_k\sin\theta)(\boldsymbol{U}_h\cos\theta - \boldsymbol{U}_k\sin\theta) + (c_h\sin\theta + c_k\cos\theta)(\boldsymbol{U}_h\sin\theta + \boldsymbol{U}_k\cos\theta) \\ &= c_h\boldsymbol{U}_h\cos^2\theta + c_k\boldsymbol{U}_k\sin^2\theta + c_h\boldsymbol{U}_h\sin^2\theta + c_k\boldsymbol{U}_k\cos^2\theta \pm c_h\boldsymbol{U}_k\sin\theta\cos\theta \pm c_k\boldsymbol{U}_h\sin\theta\cos\theta \\ &= c_h\boldsymbol{U}_h(\cos^2\theta + \sin^2\theta) + c_k\boldsymbol{U}_k(\sin^2\theta + \cos^2\theta) \\ &= c_h\boldsymbol{U}_h + c_k\boldsymbol{U}_k \end{aligned}$$

A rotation in two-dimensional subspace of h and k has no effect in other dimensions, as the orthonormal property of SVD guarantees. Multiple steps of rotations can be carried out in many two-dimensional subspaces consecutively to achieve a multi-dimensional rotation. A new solution set derived from a rotation retains the orthonormal property of SVD. The rotation in the Euclidean subspace established by SVD does not change the comparison among the core data of protein structures. Rather it converts one solution set $\mathbf{A} = \mathbf{UWV}^{\mathrm{T}}$ to other alternative solutions $\mathbf{A} = \mathbf{RST}^{\mathrm{T}}$ so that an appropriate perspective can be found to elucidate the relationship between the core data and metadata clearly and concisely.

For example, if one physical parameter could be reoriented along a single dimension k but not involving other dimensions by a rotation, it would be convincing to show that the left singular vector $\boldsymbol{U}_k$ of this dimension illustrates the structural impact by this physical parameter. Before this rotation, the same physical parameter may appear to cause structural variations along several dimensions, which leads to a difficult interpretation. Would a proper rotation establish a one-on-one correspondence from all physical or chemical parameters to all the dimensions? It depends on whether each parameter induces an orthogonal structural change, that is, whether structural responses to different parameters are independent or correlated among one another. If structural changes are indeed orthogonal, it should be possible to find a proper rotation to cleanly separate them in different dimensions. Otherwise, two different rotations are necessary to isolate two correlated responses, but one at a time.

For another example, if the observed core datasets form two clusters in the conformational space, a rotation would be desirable to separate these clusters along a single dimension k but to align these clusters along other dimensions. Therefore, the component $\boldsymbol{U}_k$ is clearly due to the structural transition from one cluster to the other. Without a proper rotation, the difference between these clusters could be complicated with multiple dimensions involved. A deterministic solution depends on whether a clear correlation exists between the core data and metadata. A proper rotation may require a user decision. A wrong choice of rotation may select a viewpoint that hinders a concise conclusion. However, it would not alter the shape of the reaction trajectory, nor create or eliminate an intrinsic structural feature. A wrong choice of rotation cannot eliminate the fact that a large gap exists between two clusters of observed core datasets

except that these clusters are not obvious from that viewpoint. A different rotation may reorient the perspective along another direction. But the structural conclusion would be equivalent. See example of before and after a rotation in (Ren, 2016).

This rotation procedure finally connects the core crystallographic datasets to the metadata of experimental conditions and accomplishes the deconvolution of physical or chemical factors that are not always orthogonal to one another after a mathematical decomposition. SVD analysis presented in this paper employs rotations extensively except that no distinction is made in the symbols of components and coefficients before and after a rotation except in this section. This method is widely applicable in large-scale structural comparisons. Furthermore, Ren rotation after SVD is not limited to crystallography and may impact other fields wherever SVD is used. For example, SVD is frequently applied to spectroscopic data, images, and genetic sequence data.

A preliminary analysis of SVD involving all difference maps (Table S1) shows that the short and long delays are in two different subspaces (Fig. S15). That is to say, difference maps in the time regimes before 10 ps and after 10 ns share no common features. This conclusion cannot be reached without a proper rotation of the components. The separation between the short and long delays into different subspaces can only be viewed clearly from this specific perspective shown in Fig. S15. Therefore, these time regimes are analyzed separately.

Exponential fitting of SVD coefficients

The time dependencies of the SVD coefficients $c_1(t)$, $c_3(t)$, and $c_6(t)$ for the long delays > 10 ns are modeled with exponential functions (Fig. S7). Each time-dependent coefficient

$$c_k(t) = b_k + p_k \exp\left(-\frac{t}{\tau_1}\right) + q_k \exp\left(-\frac{t}{\tau_3}\right) + r_k \exp\left(-\frac{t}{\tau_6}\right) \tag{4}$$

where $k = 1$, 3, or 6. The time constant τ_k associated with the major change in each coefficient models each step in the reaction scheme K → L → M_1 → M_2. Whether the time-dependent coefficients can be successfully fitted with exponentials is also a good test for a proper rotation. Because the fact that the fractional concentrations of intermediate species can be expressed as exponentials indicate that the reaction follows a regular kinetic scheme.

Structural refinement against reconstituted dataset

The linear combination $\Delta\rho(t) = f_1(t)\boldsymbol{R}_1 + f_2(t)\boldsymbol{R}_2 + \ldots + f_n(t)\boldsymbol{R}_n$ after a rotation reconstitutes one of the observed difference maps at a specific time point t. This time-dependent difference map depicts an ever-evolving mixture of many excited species. A reconstituted difference map $\Delta\rho$(E) for a time-independent, pure, excited species E = intermediate I′, I, J′, and J deconvoluted from many mixtures would take the same form except that only one or very few coefficients remain nonzero if a proper rotation has been found (Table S2). In order to take advantage of the mature refinement software for macromolecular structures with extensive stereochemical restraints, a set of structure factor amplitudes is needed. Therefore, it is necessary to reconstitute a set of structure factor amplitudes that would produce the target difference map $\Delta\rho$(E) based on a known structure at the ground state. First, an electron density map of the structure at the ground state is calculated. This calculated map is used as a base map. Second, this base map of the ground state is combined with the positive and negative densities in the target difference map $\Delta\rho$(E) so that the electron densities at the ground state are skewed toward the intermediate state. Third, structure factors are calculated from the combined map. Finally, the phase set of the calculated structure factors is discarded, and the amplitudes are used to refine a single conformation of the intermediate species E that $\Delta\rho$(E) represents.

This protocol following the SVD and Ren rotation of components achieves a refinement of a pure structural species without the need of alternative conformations. Several points are noteworthy. First, the minimization protocol in this refinement is performed against a numerically reconstituted amplitude set that has never been directly measured from a crystal. This reconstituted dataset could be considered as an extrapolated dataset "on steroids" if compared to the traditional extrapolation of small differences, such as, the Fourier coefficient set to calculate a 3Fo-2Fc map, a technique often used to overcome a partial occupancy of an intermediate structure. An extrapolation of small differences is not directly observed either but computed by an exaggeration of the observed difference based on an assumption that the intermediate state is partially occupied, such as the doubling of the observed difference in 3Fo-2Fc = Fo + 2(Fo-Fc). In contrast to the conventional technique of extrapolation, the deconvolution method applied here is an interpolation among many experimental

datasets rather than an extrapolation. Secondly, the deconvolution is a simultaneous solution of multiple intermediate states mixed together instead of solving a single excited state.

Second, a map calculated from the ground state structure is chosen as the base map instead of an experimental map such as Fo or 2Fo-Fc map. If the second step of the protocol is skipped, that is, no difference map is combined with the ground state map, the refinement would result in an *R* factor of nearly zero, since the refinement is essentially against the calculated structure factors (bR in Table S2). This is to say, the residuals of the refinement are solely due to the difference component instead of the base map. This is desirable since errors in the static structure of the ground state are gauged during its own refinement. On the other hand, if an experimental map is chosen as a base map, the refinement *R* factors would reflect errors in both the base map and the difference map, which leads to a difficulty in an objective evaluation of this refinement protocol.

Third, the combination of the base map and a difference map is intended to represent a pure intermediate species. Therefore, alternative conformations in structural refinement that model a mixture of species would defeat this purpose. However, this combined map could be very noisy and may not represent a single species without a proper rotation. This is particular the case, if the target difference map $\Delta\rho$ is not derived from an SVD analysis and Ren rotation. The SVD analysis identifies many density components that are inconsistent among all observed difference maps and excludes them, which greatly reduces the noise content. Therefore, this refinement protocol may not be very successful without an SVD analysis. Another source of noise originates from the phase set of the structure factors. Prior to the refinement of the intermediate structure, the phase set remains identical to that of the ground state. This is far from the reality when an intermediate structure involves widespread changes, such as those refined in this study. If the rotation after SVD is not properly selected, the target difference map would remain as a mixture minus the ground state. Therefore, the refinement of a single conformation would encounter difficulty or significant residuals, as judged by the *R* factors, the residual map, and the refined structure. A proper solution to this problem is a better SVD solution by Ren rotation rather than alternative conformations. A successful refinement of near perfect

trans or *cis* double bonds is a good sign to indicate that the reconstituted amplitude set after a rotation reflects a relatively homogeneous structure. If a double bond could not be refined well to near perfect *trans* or *cis* configuration, the dataset of structure factor amplitudes is likely from a mixture of heterogeneous configurations, which occurred frequently in previous studies of bR and photoactive yellow protein (Jung et al., 2013; Lanyi and Schobert, 2007; Nogly et al., 2018). It has been a great difficulty in crystallographic refinement in general that a heterogeneous mixture of conformations cannot be unambiguously refined even with alternative conformations. This difficulty becomes more severe when a mixture involves more than two conformations or when some conformations are very minor.

Lastly, the refinement protocol proposed here could be carried out in the original unit cell and space group of the crystal at the ground state. However, this is not always applicable as the original goal of the meta-analysis is a joint examination of all available structures from a variety of crystal forms. It would be highly desirable to evaluate difference maps of the same or similar proteins from non-isomorphous crystals together by SVD. Alternatively, the refinement protocol could also be performed in the space group of P1 with a virtual unit cell large enough to hold the structure, which is the option in this study (Table S2). This is to say, the entire analysis of SVD-rotation-refinement presented here could be extracted and isolated from the original crystal lattices, which paves the way to future applications to structural data acquired by experimental techniques beyond crystallography, most attractively, to single particle reconstruction in cryo electron microscopy.

Supplementary Tables

Table S1. Datasets analyzed in this work

Publication	PDB	Label	Resolution	Main conclusions	New findings in this work
Nango et al. Science 354, 1552, 2016	5b6v	dark5	1.77 Å	A newly ordered water on the CP side bridges the SB to Thr89 after isomerization, thus further conducts a proton to Asp85.	These datasets contribute to the overdetermination of the structures K → L → M_1 → M_2. The early creased retinal is flattened; C_{20} methyl group returns into the original plane of the resting retinal as K transitions to L. The most flattened chromophore is achieved in L. The EC half channel contracts in L while the CP half channel starts to open. Reprotonation of the SB starts in L. Several ordered waters are observed in the enlarged CP half channel in M_1. The SB move toward inboard in M_1 and M_2.
	5b6w	16ns	2.0 Å		
	5h2h	40ns	2.0 Å		
	5h2i	110ns	2.0 Å		
	5h2j	290ns	2.0 Å		
	5b6x	760ns	2.0 Å		
	5h2k	2μs	2.0 Å		
	5h2l	5.25μs	2.0 Å		
	5h2m	13.8μs	2.0 Å		
	5b6y	36.2μs	2.0 Å		
	5h2n	95.2μs	2.0 Å		
	5h2o	250μs	2.0 Å		
	5h2p	657μs	2.0 Å		
	5b6z	1.725ms	2.0 Å		
Nogly et al. Science 361, eaat0094, 2018	6g7h	dark6	1.5 Å	Retinal fully isomerizes at 10 ps. But the SB water dissociates earlier.	The short-delay datasets contribute to the structures of I′ → I → J′ → J. Photoisomerization in J′; retinal binding pocket expansion before 1 ps in I and contraction at 10 ps in J
	6g7i	49-406fs	1.9 Å		
	6g7j	457-646fs	1.9 Å		
	6g7k	10ps	1.9 Å		
	6g7l	8.33ms	1.9 Å		
Kovacs et al. Nat. Commun. 10, 3177, 2019	6ga1	dark1	1.7 Å	The exceedingly high power density of the pump laser causes two-photon absorption. Vibrational motions were observed.	The sub-ps datasets exhibit extensive vibrations at various frequencies. The vibrational signals are widespread over the entire bR molecule and not associated with any structural elements. Therefore, it is concluded that these global vibrations are intrinsic properties of bR induced by short laser pulses. The vibrational signals are more prominent under higher power density of the laser pulses. However, these vibrations are irrelevant to the light-driven proton pumping function of bR.
	6ga2	dark2	1.8 Å		
	6rmk	dark3	1.8 Å		
	6ga7	240fs	1.8 Å		
	6ga8	330fs	1.8 Å		
	6ga9	390fs	1.8 Å		
	6gaa	430fs	1.8 Å		
	6gab	460fs	1.8 Å		
	6gac	490fs	1.8 Å		
	6gad	530fs	1.8 Å		
	6gae	560fs	1.8 Å		
	6gaf	590fs	1.8 Å		
	6gag	630fs	1.8 Å		
	6gah	680fs	1.8 Å		
	6gai	740fs	1.8 Å		
	6ga4	1ps	1.8 Å		
	6ga5	3ps	1.9 Å		
	6ga6	10ps	1.8 Å		
	6ga3	33ms	2.1 Å		
Weinert et al. Science 365, 61, 2019	6rqp	dark	1.8 Å	Helices E and F swing outward after 10 ms.	These datasets contribute to the overdetermination of M_2, in which an open CP half channel is observed. The SB moves toward inboard.
	6rnj	0-5ms	2.6 Å		
	6rph	10-15ms	2.6 Å		
	6rqo	activated	2.0 Å		

1585

Table S2. Refinement statistics

Intermediate		bR	I′	I	J′	J	K	L	M_1	M_2
Time period		0-	< 50 fs	40-700 fs	0.5-2 ps	1-30 ps	3 ps-2 μs	1-100 μs	10-1000 μs	0.5-5 ms
Short delay components	$\boldsymbol{U}_{10}$			3,300		-4,200				
	$\boldsymbol{U}_{14}$		2,000	2,700	2,700	2,000				
	$\boldsymbol{U}_{17}$		3,000		-1,300	-300				
Long delay components	$\boldsymbol{U}_{1}$						-700		2,200	1,000
	$\boldsymbol{U}_{2}$						1,800	1,800	1,800	1,200
	$\boldsymbol{U}_{3}$						-1,000	2,100	1,500	900
	$\boldsymbol{U}_{6}$							-600		1,500
Starting model		PDB 6g7h								
Resolution range		50-2.1 Å								
Space group		P1								
Unit cell		a = 62.32 Å; b = 62.32 Å; c = 111.10 Å; α = 90°; β = 90°; and γ = 120°								
Unique reflections		80,354 in working set + 4,236 in test set = 84,590 total								
Completeness		95% in working set + 5% in test set = 100% reconstituted								
R (%)		1.8	29.4	31.0	29.1	30.0	26.0	27.7	28.4	28.5
R_{free} (%)		1.9	31.1	32.4	30.4	30.7	26.3	28.8	29.6	29.7
Refined content		230 protein residues + 1 retinal + water molecules								
Number of atoms		1,798	1,795	1,798	1,796	1,795	1,798	1,794	1,799	1,796
Water molecules		8	5	8	6	5	8	4	9	6
RMSD bonds (Å)		0.005	0.009	0.009	0.009	0.009	0.009	0.009	0.009	0.009
RMSD angles (°)		0.793	1.206	1.105	1.085	1.068	1.006	1.074	1.120	1.081
Rama. favored (%)		98.7	96.5	95.6	96.1	96.5	97.8	96.5	97.4	96.1
Rama. outliers (%)		0.0	0.0	0.4	0.4	0.4	0.4	0.0	0.0	0.4
Clash score		4	9	5	4	6	6	7	10	7

1586

1587

Supplementary Figures and Legends

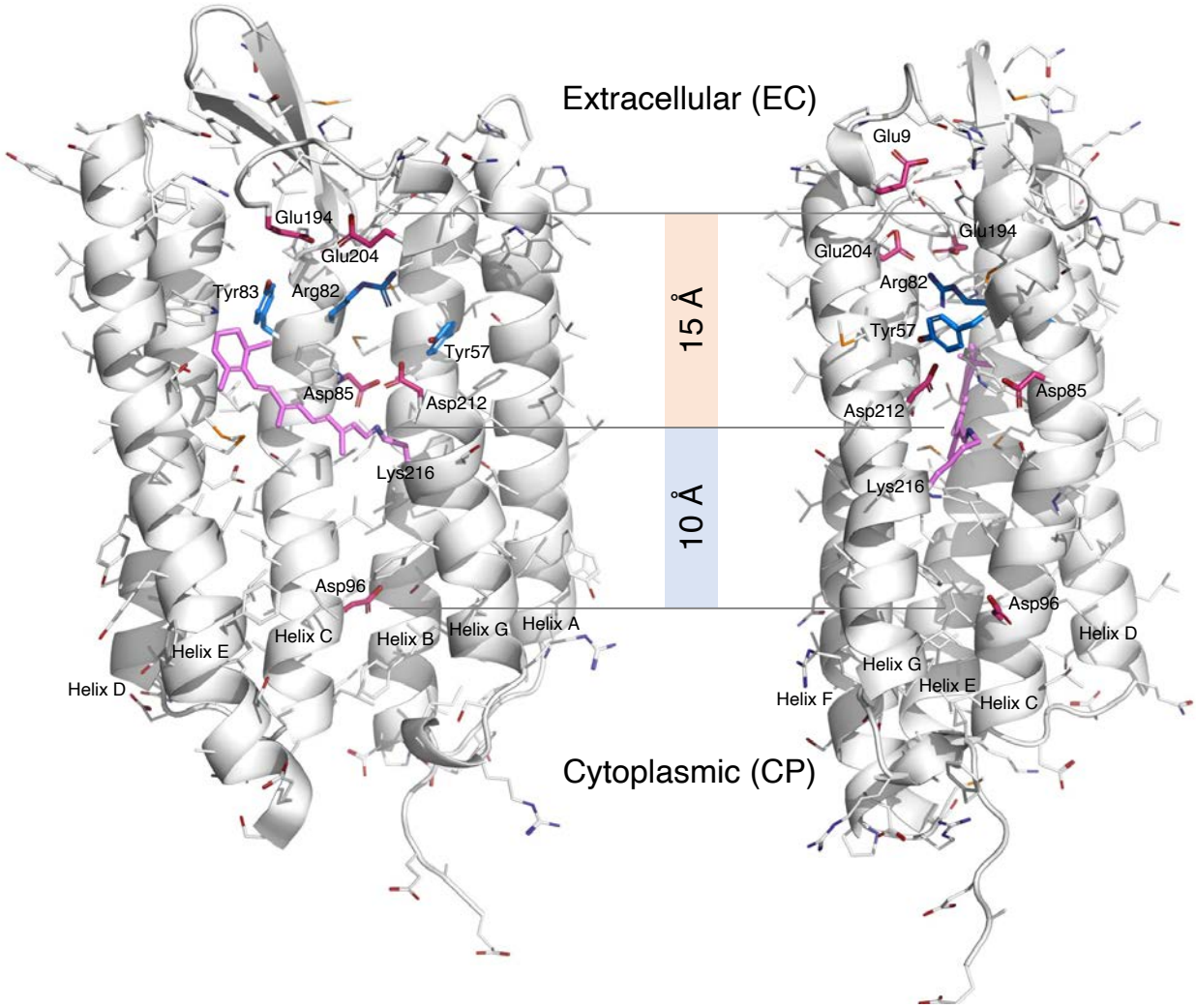

Figure S1. Orthographical views of EC and CP half channels. Parts of the structure are omitted to reveal the interior. The acidic residues in the half channels are highlighted in red. Those in the EC half channel are deprotonated. Asp96 in the hydrophobic CP half channel could be protonated (Gerwert et al., 1989). Arg82 in blue is protonated at neutral pH to form a positive charged guanidinium ion with a pK_a of 12.5. Tyr57 and 83 with a pK_a of 10 in blue could be deprotonated at alkaline pH.

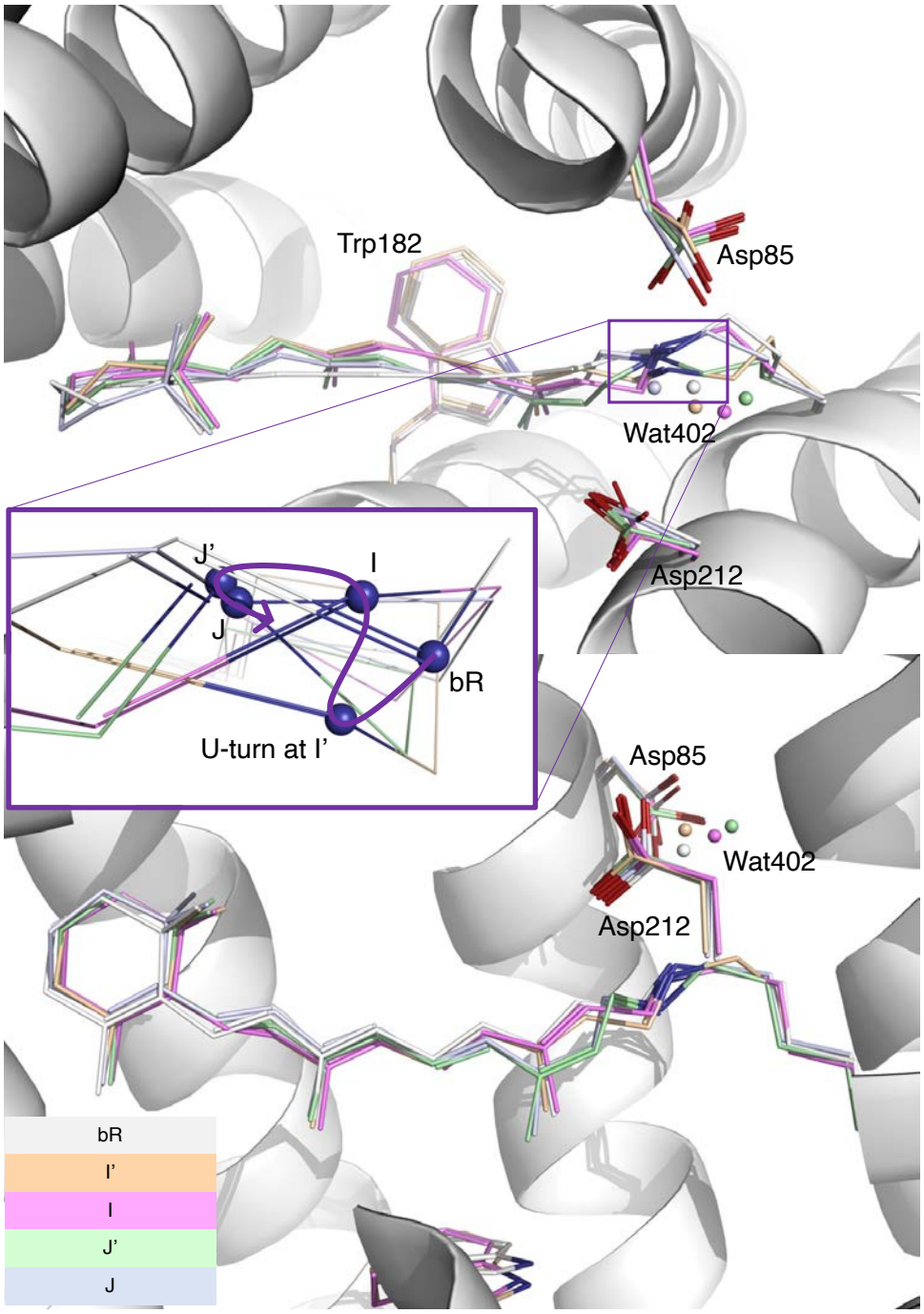

Figure S2. Two orthographical views of early intermediates. The refined conformations of the retinal and several key side chains are rendered in stick models of various colors. These early intermediates are compared with the resting state in white ribbon and stick model. Wat402 is rendered in small spheres. A zoom-in view of the SB is presented in the inset. N_ζ is shown in blue spheres. Its trajectory marked by a spline curve shows a

sharp U-turn at I′ state. The SB moves toward the distal direction during I and J due to a creased retinal (Fig. 2b).

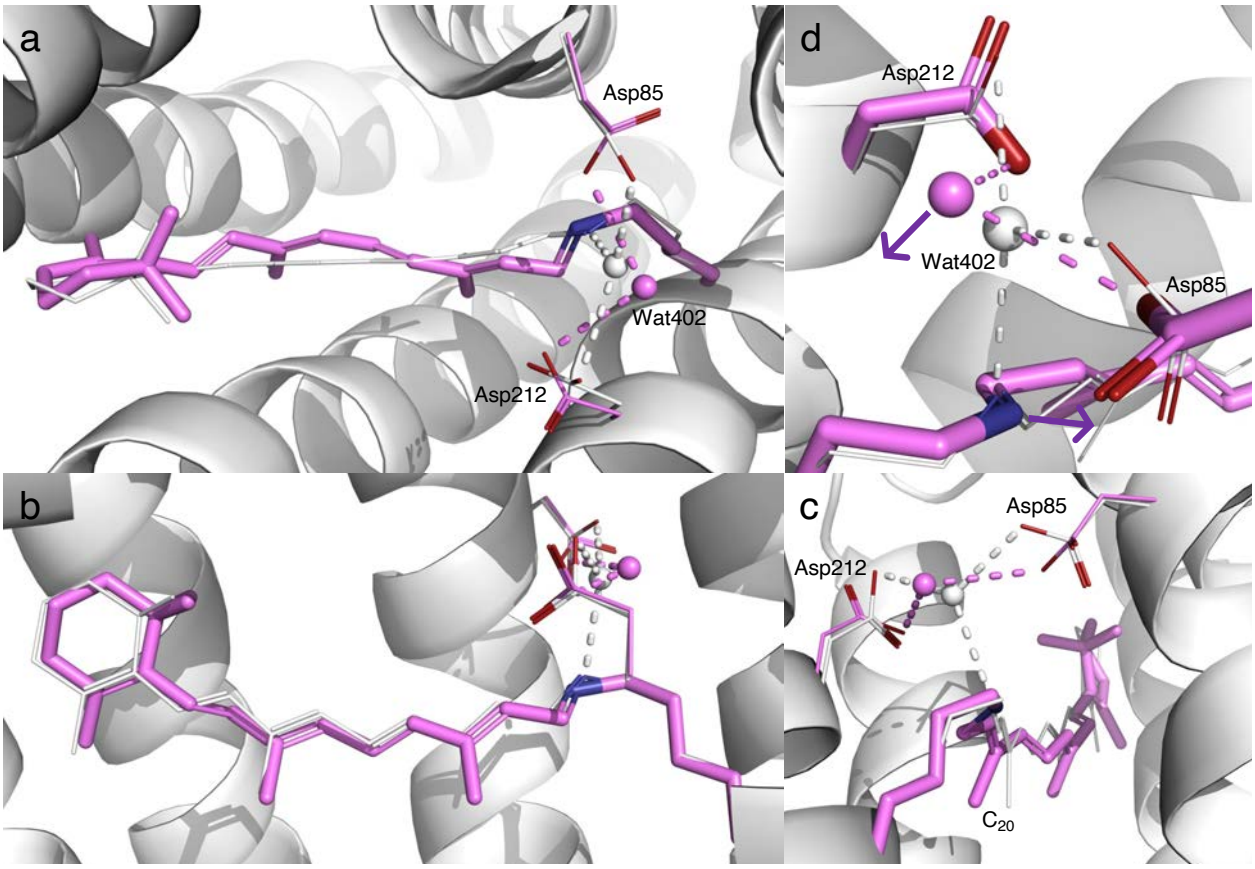

Figure S3. Refined structure of I state. (a, b, and c) Three orthographical views of retinal in I state. The refined retinal conformation in purple is compared with the resting state in white. The SB is pointing toward inboard with a perfect *syn* conformation at the single bond N_ζ-C_ε. C_{20} methyl group remains tilted toward outboard. Wat402 with good electron density is displaced toward outboard and remains H-bonded with both Asp85 and 212. (d) Zoom-in view of SB and Wat402. Wat402 is 3.7 Å away from the SB N_ζ. The would-be H-bond directions of the SB and Wat402 are pointing toward the opposite directions as marked by the arrows. This geometry makes not only a H-bond impossible but also any proton transfer difficult.

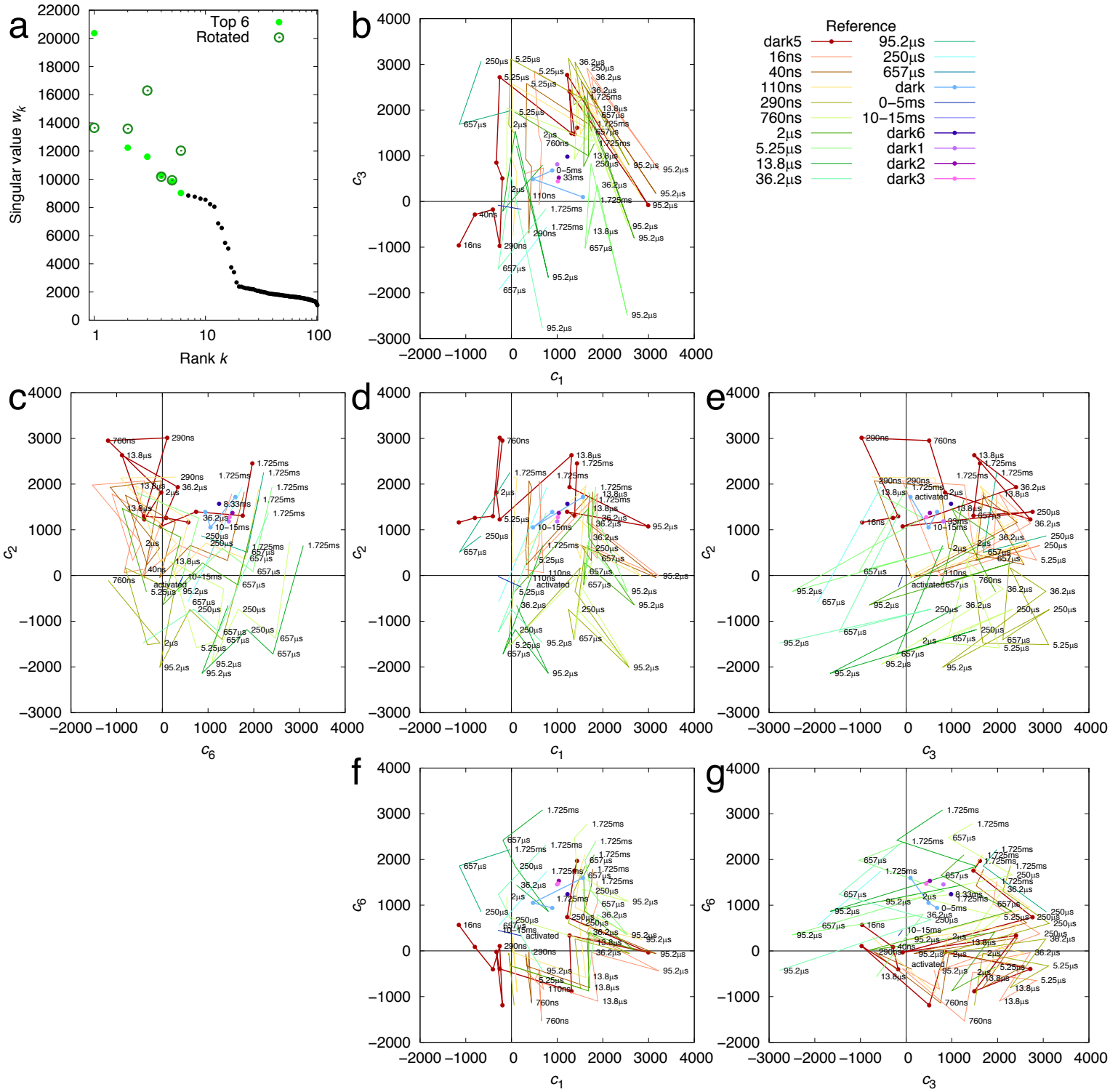

Figure S4. SVD analysis of difference Fourier maps at long delays > 10 ns. SVD analyses of difference Fourier maps result in time-dependent coefficients $c_k(t)$, where k =

1, 2, …, each corresponding to a time-independent components $\boldsymbol{U}_k$. Each raw difference map at a time delay t can be closely represented by a linear combination of these components, $c_1(t)\boldsymbol{U}_1 + c_2(t)\boldsymbol{U}_2 + \ldots$, that is called a reconstituted difference map. Each of these components $\boldsymbol{U}_k$ and the reconstituted difference maps can be rendered in the same way as an observed difference map. The coefficient set $c_k(t)$ is therefore a trace of the photocycle trajectory, when these time-dependent functions are plotted in a multi-dimensional space or plotted together against the common variable t. See Methods for detail. (a) Singular values before and after rotation (Ren, 2019, 2021). 19 components stand out. (b-g) Time-dependent coefficients of four components $\boldsymbol{U}_1$, $\boldsymbol{U}_2$, $\boldsymbol{U}_3$, and $\boldsymbol{U}_6$. Each pair of the adjacent orthographical views, horizontal or vertical, can be folded along a straight line between them to erect a three-dimensional space. Each colored trace represents difference maps in a time series calculated with a common reference. Those time series with a dark reference are plotted with thick lines with dots. Other series are in thin lines without dots.

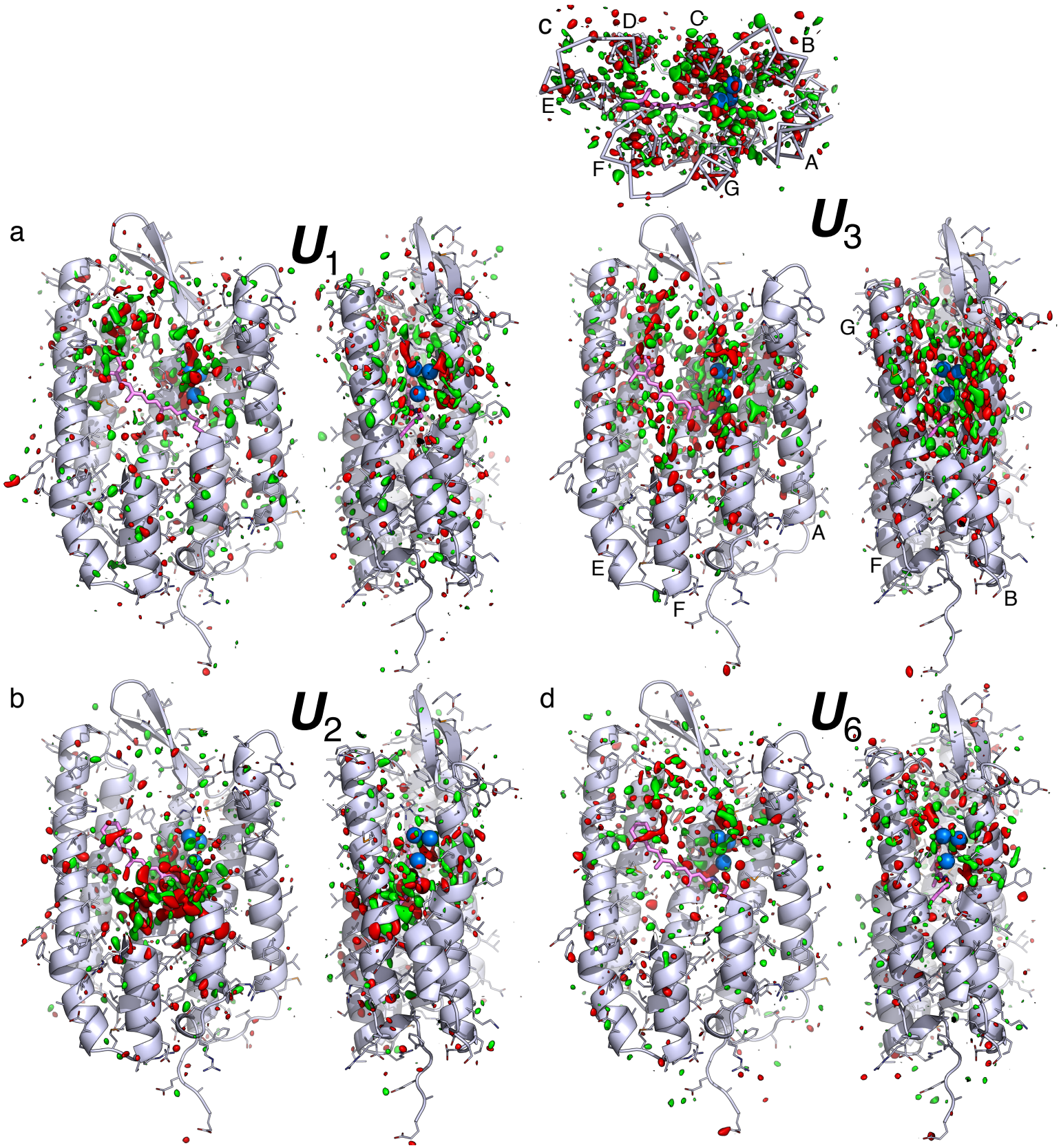

1643

Figure S5. Component maps $\boldsymbol{U}_1$, $\boldsymbol{U}_2$, $\boldsymbol{U}_3$, and $\boldsymbol{U}_6$ from long delays. The main chain and side chains of the protein are rendered with ribbons and sticks, respectively. The retinal and Lys216 are in purple sticks. Several key waters are in blue spheres. Parts of the structure are omitted to reveal more of the interior. The maps are contoured at $\pm 3\sigma$ in green and red, respectively. (a) Two orthographical views of $\boldsymbol{U}_1$. The signals are distributed over the EC half of the molecule. (b) Two orthographical views of $\boldsymbol{U}_2$. The signals are concentrated around the proximal segment of the retinal. (c) Three orthographical views of $\boldsymbol{U}_3$. Widespread signals are associated with all seven helices. (d) Two orthographical views of $\boldsymbol{U}_6$. The signals are over the EC half of the molecule.

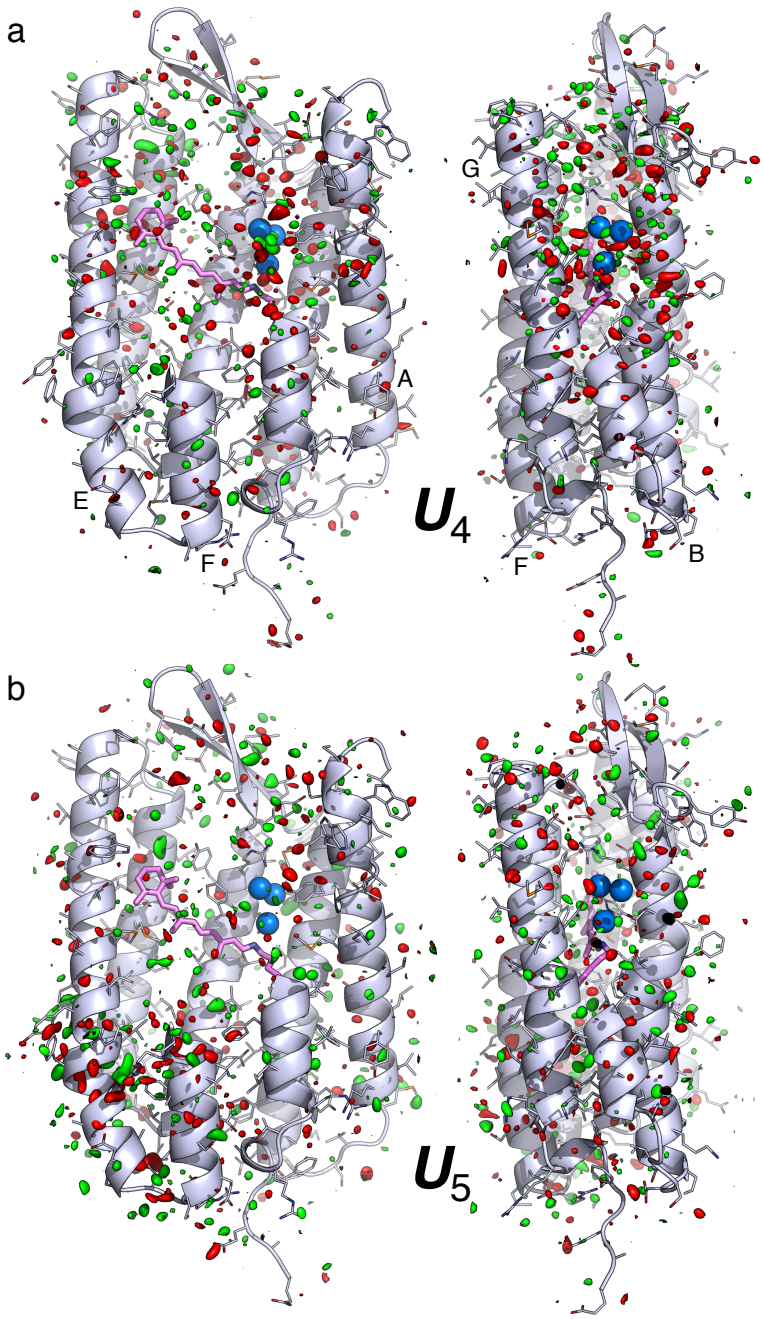

Figure S6. Component maps $\boldsymbol{U}_4$ and $\boldsymbol{U}_5$ from long delays. The main chain and side chains of the protein are rendered with ribbons and sticks, respectively. The retinal and Lys216 are in purple sticks. Several key waters are in blue spheres. Parts of the structure are omitted to reveal more of the interior. The maps are contoured at $\pm 3\sigma$ in green and red, respectively. These components are not associated with a clear time dependency. Therefore, they are isolated but not used in structure refinement. (a) Two orthographical views of $\boldsymbol{U}_4$. Some signals are distributed over the EC half of the

molecule. (b) Two orthographical views of $\boldsymbol{U}_5$. Some signals are located around the CP segments of helices E and F.

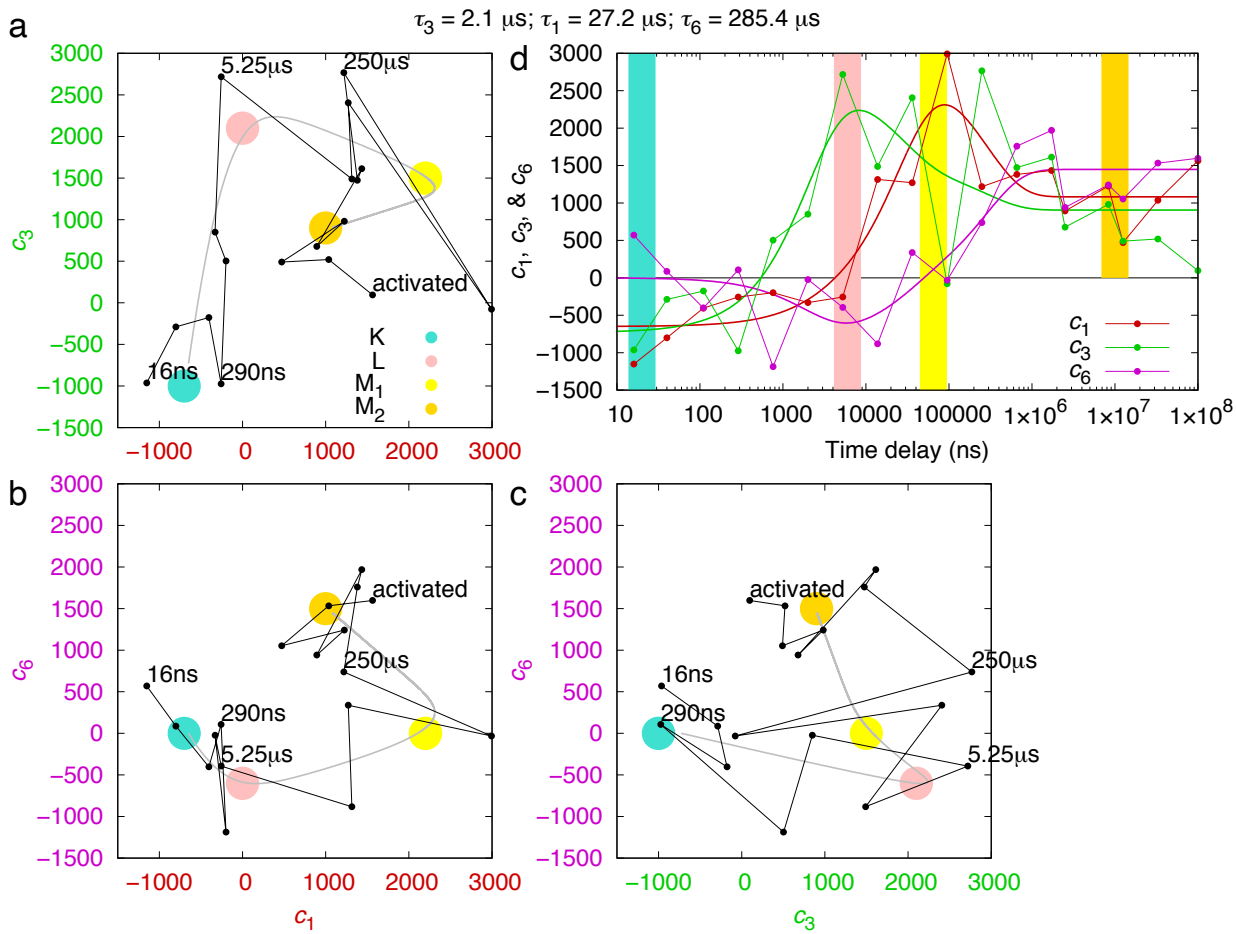

Figure S7. Exponential fitting of SVD coefficients of long delays. (a, b, and c) The time dependencies of the SVD coefficients $c_1(t)$, $c_3(t)$, and $c_6(t)$ of the long delays are modeled with exponential functions (Methods). The time constant τ_k associated with the major change in each coefficient models a step in the reaction scheme K → L → M_1 → M_2. τ_3 = 2.1±1 μs or a rate of 470 ms^{-1} is the rate of increase in $c_3(t)$. τ_1 = 27±10 μs or a rate of 37 ms^{-1} describes the jump in $c_1(t)$. τ_6 = 290±100 μs or a rate of 4 ms^{-1} seems to separate M_1 and M_2. The fitted exponential functions are plotted as the gray curves through the black dots derived from SVD in three orthographical views of the three-dimensional subspace of c_1, c_3, and c_6. The large colored dots mark the relatively pure states of K, L, M_1, and M_2. (d) SVD coefficients and their exponential fittings as functions of time. The relatively pure states are marked as color bars at the approximate time. The result of exponential fitting shows the time-dependency clearer. The second component map $\boldsymbol{U}_2$ seems to be a constant component without a time-dependent trend (Fig. S4cde). It describes significant changes near the SB and the retinal anchor (Figs. 3ab and S5b). The

third component map $\boldsymbol{U}_3$ increases sharply and consistently around 1 μs (Figs. S4beg). This component contains widespread signals associated with all seven helices (Fig. S5c), therefore describes the global changes during K → L transition. The first component $\boldsymbol{U}_1$ increases at 10 μs (Figs. S4bdf), which could reflect the changes during L → M transition. $\boldsymbol{U}_1$ clearly contains signals over the EC half of the molecule (Fig. S5a), which indicates events related to the proton release. Similarly, the sixth component $\boldsymbol{U}_6$ also shows additional signals on the EC half to a lesser extent (Fig. S5d). This component seems to increase at a rather late time around hundreds of μs (Figs. S4cfg), which splits the M state into M_1 and M_2.

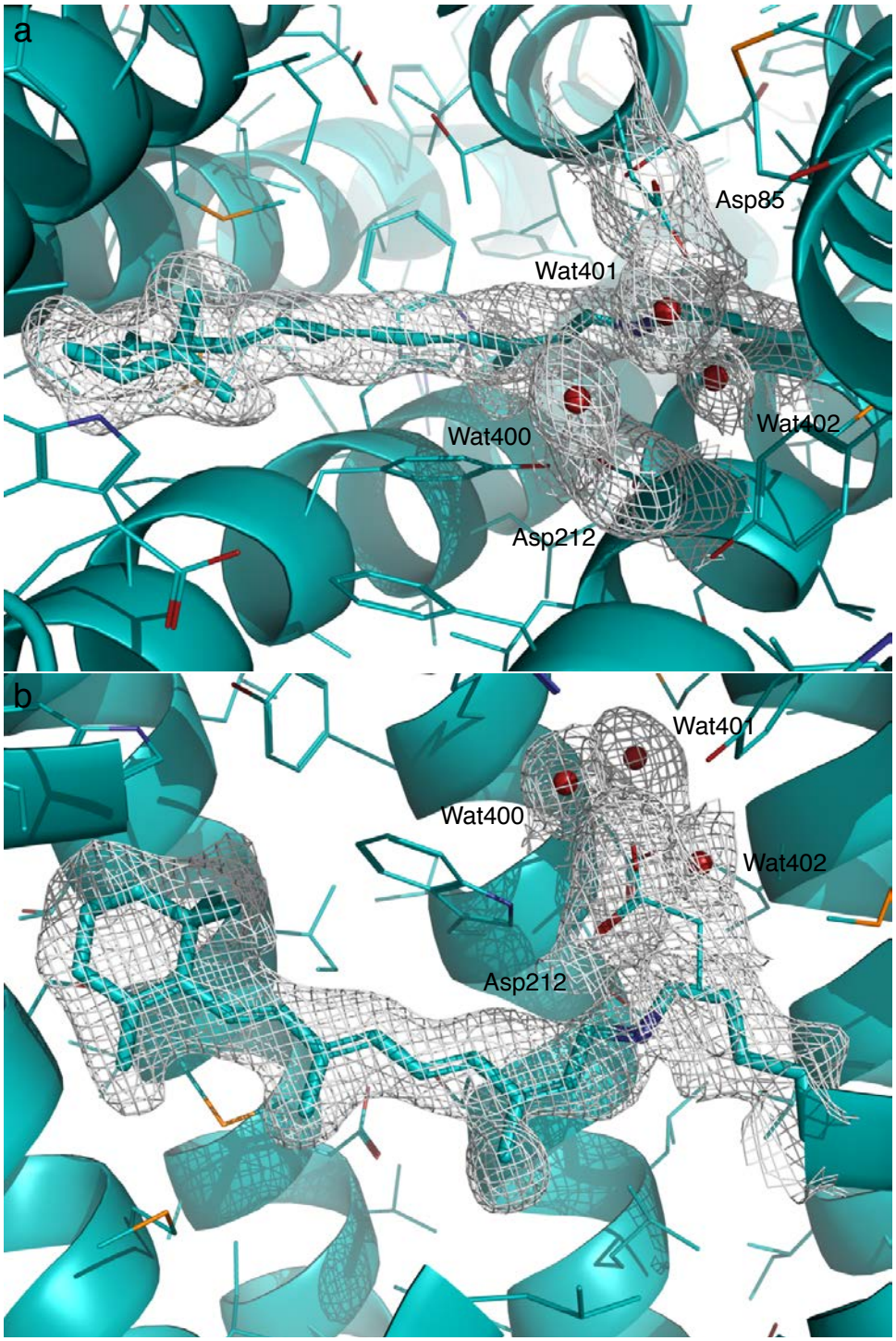

Figure S8. Two orthographical views of the 2Fo-Fc map of K contoured at 6σ. Here Fo is the reconstituted structure factor amplitudes rather than observed amplitudes (Table S2). Fc is the structure factor amplitudes calculated from the refined structure (Methods). The same applies to the other 2Fo-Fc maps.

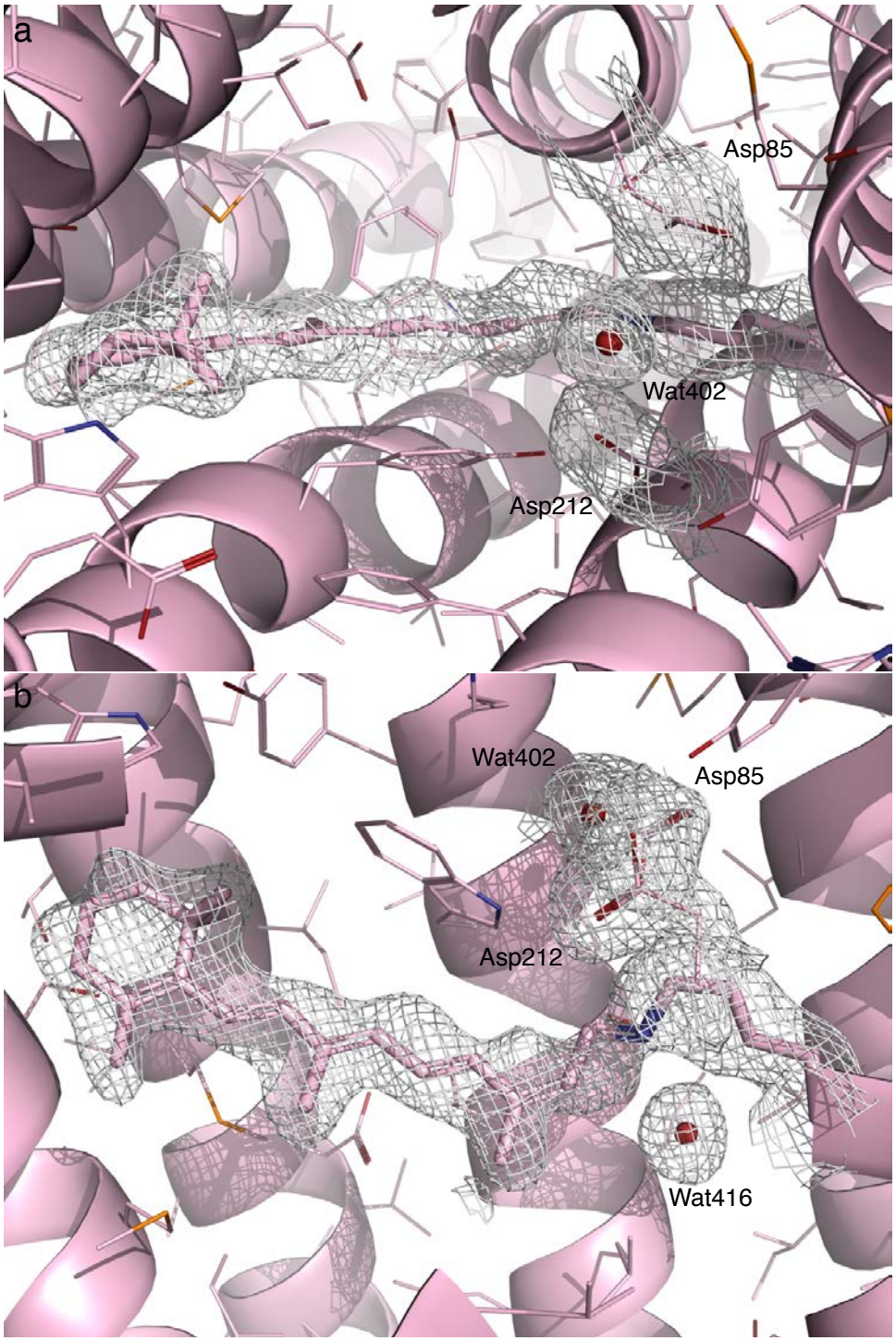

Figure S9. Two orthographical views of the 2Fo-Fc map of L contoured at 3.5σ. Here Fo is the reconstituted structure factor amplitudes rather than observed amplitudes (Table S2). Fc is the structure factor amplitudes calculated from the refined structure (Methods).

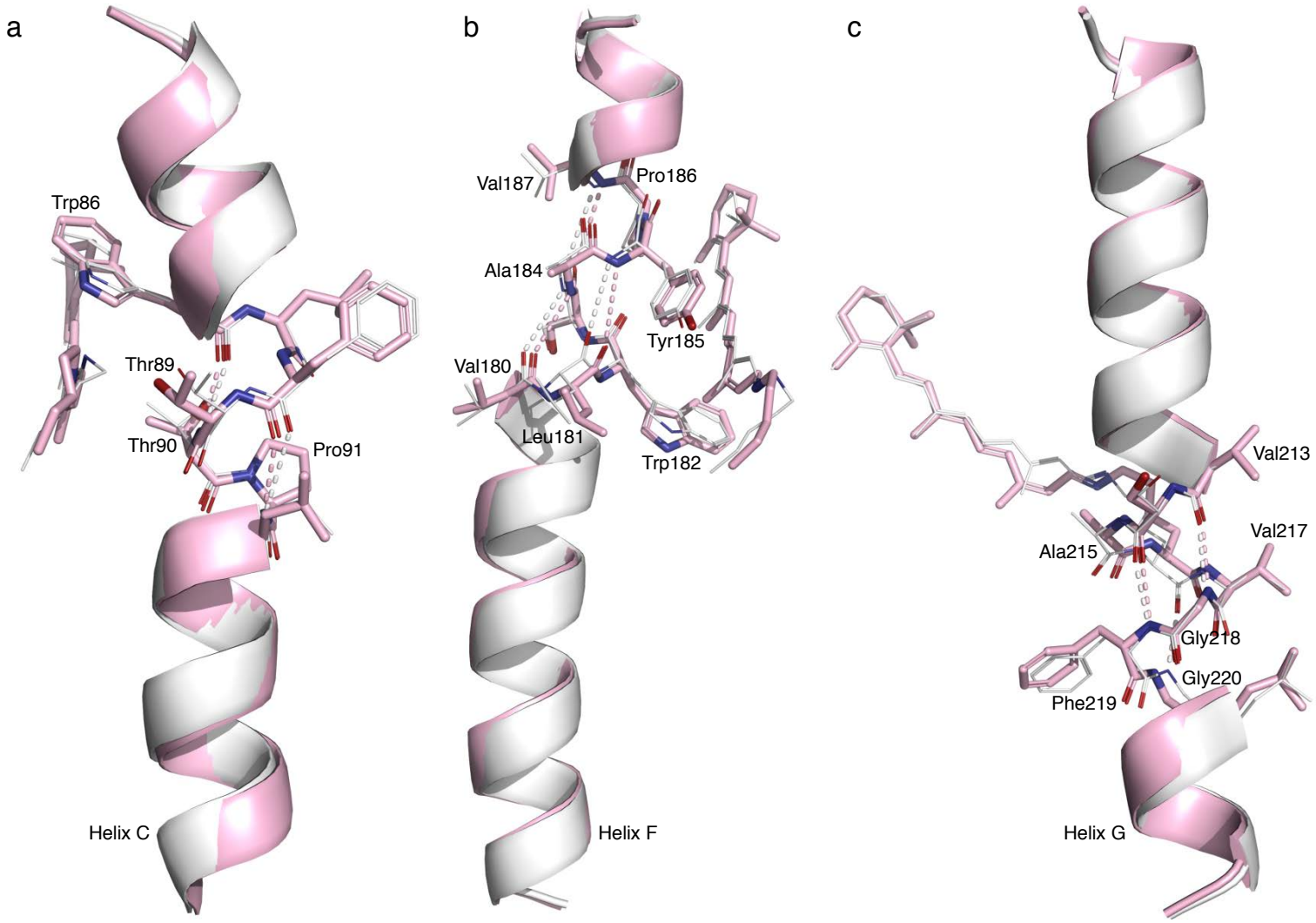

Figure S10. Irregularities in helices C, F, and G. bR in the resting state and L are rendered in white and pink, respectively. (a) Kinked helix C. All main chain H-bonds are regular except that Pro91 in helix C causes a kink. This kink was noticed as soon as the bR structure was determined to a reasonable resolution (Grigorieff et al., 1996). In the resting retinal, the corner of C_ε makes a contact with Thr89 and pushes the helix inboard. In bR, J, K, and L, C_ε moves more and more outboard (Fig. 3f). So does Thr89. The opposite motions occur in L, M_1, M_2, and back to bR (Fig. 4c). Thr90 also contributes to the seal. Pro91 is located exactly at right place to facilitate this spring-loaded bend. (b) Stretched helix F. Pro186 removes one H-bond in helix F. Several would-be H-bonds in the main chain around Pro186 are stretched to 3.6-4.2 Å in the resting state, such as Val180O-Ala184N, Leu181O-Tyr185N, and Ser183O-Val187N.

Pro186 and these stretched H-bonds marked by dashed lines effectively breaks helix F into two segments. In J, K, and L, Trp182 is pushed by C_{20} methyl group more and more toward the CP. The breakage in helix F stretches even more. P186L mutant is likely to feature an intact α helix F with uninterrupted main chain H-bonds. Its proton pumping activity is severely affected (Hackett et al., 1987). A more rigid helix F would increase the difficult to displace Trp182 toward the CP direction and hinder the opening of the CP half channel for proton uptake. (c) π helical segment in helix G. The retinal anchor is in a π helical segment with two main chain H-bonds Val213O-Gly218N and Ser214O-Phe219N. Unlike the regular α helix, a π helix features H-bonds from the carbonyl of residue *n* to the amide N of residue *n*+5. During the transition from the α helix to the π helical segment, Val217N does not have a H-bond partner. As the π helical segment transitions back to the regular α helical conformation, Ala215O does not join the H-bond pattern for helical formation. Loss of main chain H-bonds on both sides of the retinal anchor allows the anchor to move 1.2 Å in L. In addition, two nearby Gly218 and 220 increase the flexibility of the anchor.

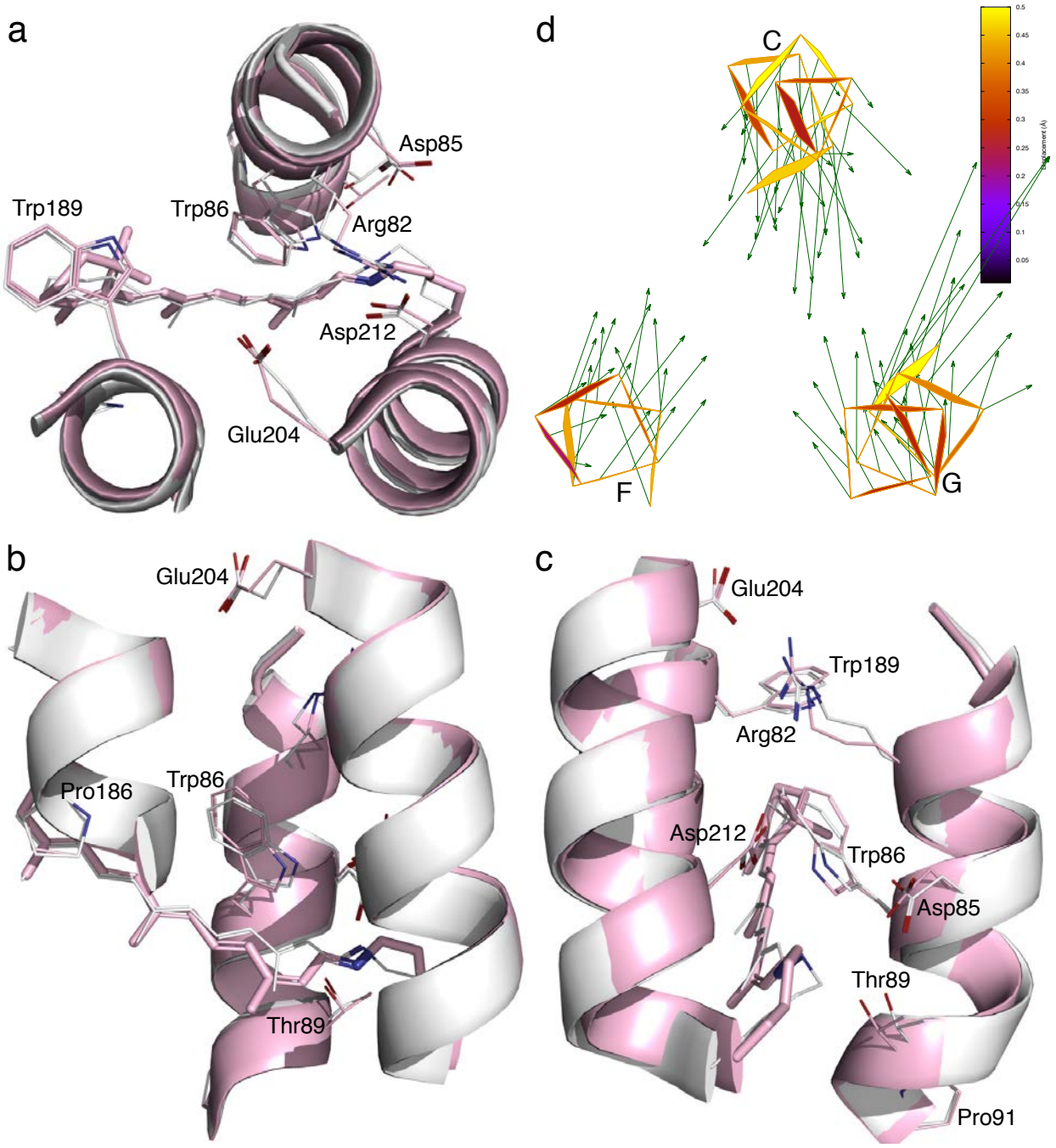

Figure S11. Tighter EC half channel in L. (a-c) Three orthographical views of the EC half channel. The resting state and L state are rendered in white and pink, respectively. (d) Atomic displacements in the main chain around the EC half channel from the resting state to L are marked with arrows 10× as long as the actual values.

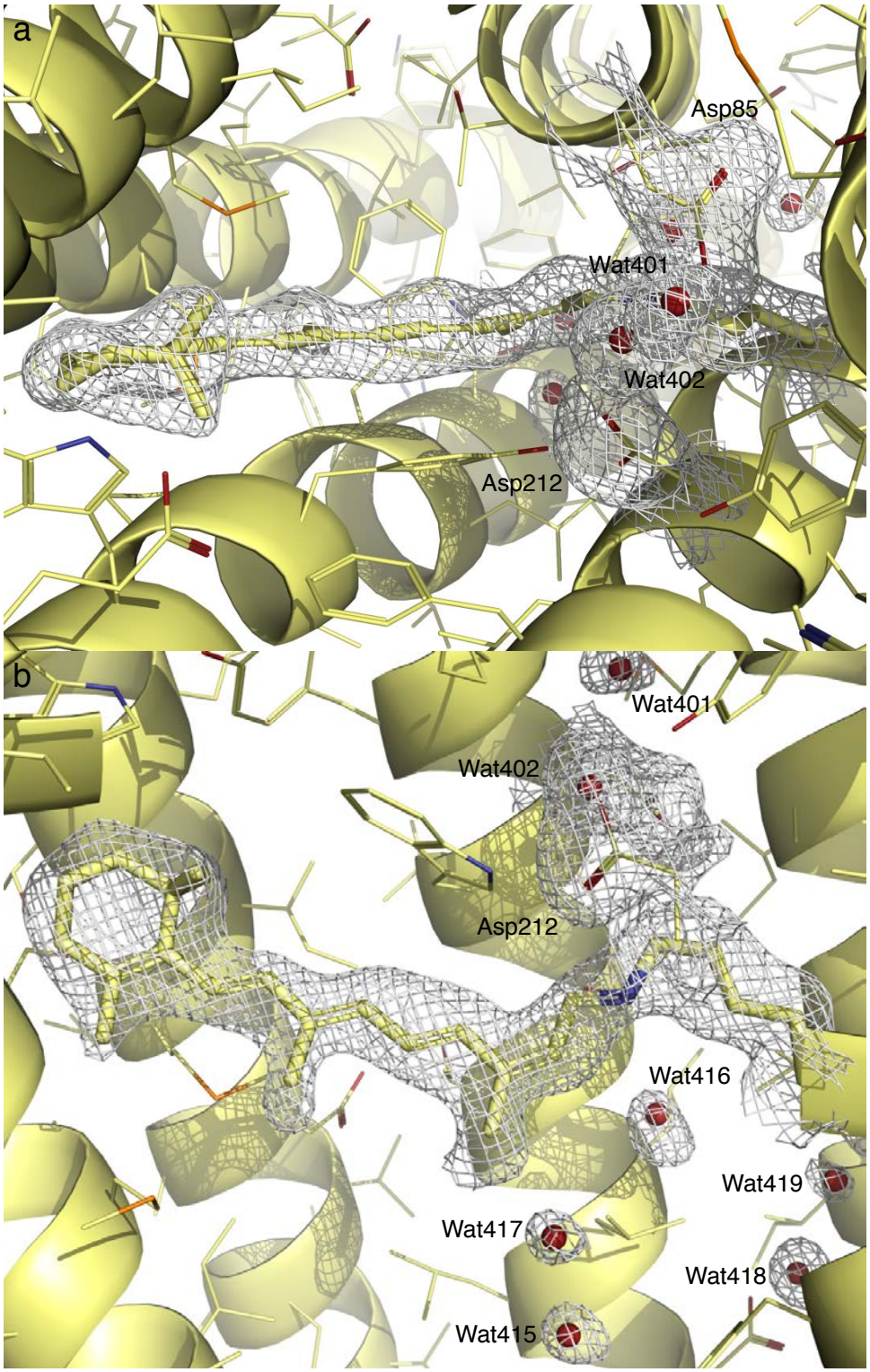

Figure S12. Two orthographical views of the 2Fo-Fc map of M_1 contoured at 3σ. Here Fo is the reconstituted structure factor amplitudes rather than observed amplitudes

(Table S2). Fc is the structure factor amplitudes calculated from the refined structure (Methods).

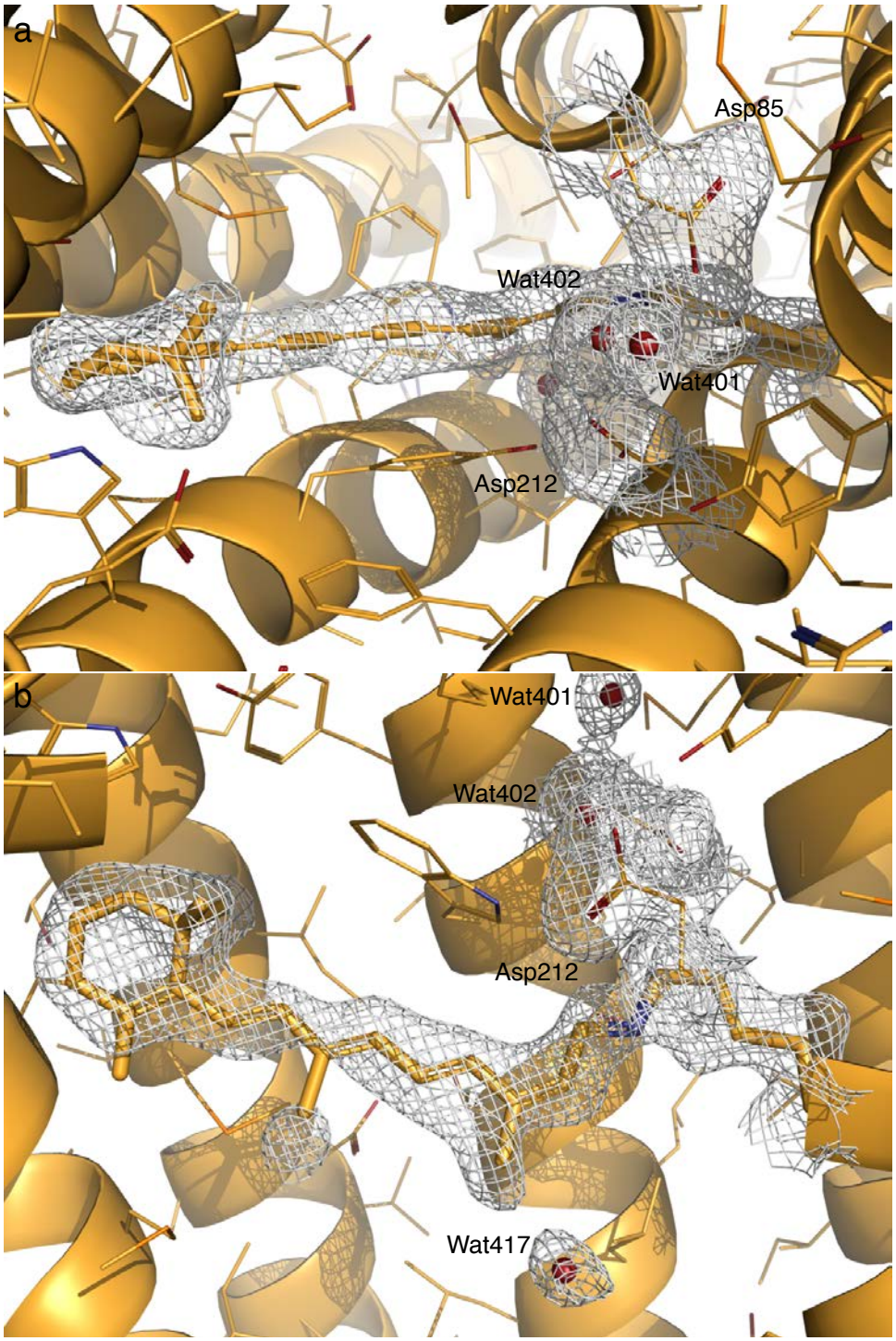

Figure S13. Two orthographical views of the 2Fo-Fc map of M_2 contoured at 5σ. Here Fo is the reconstituted structure factor amplitudes rather than observed amplitudes (Table S2). Fc is the structure factor amplitudes calculated from the refined structure (Methods).

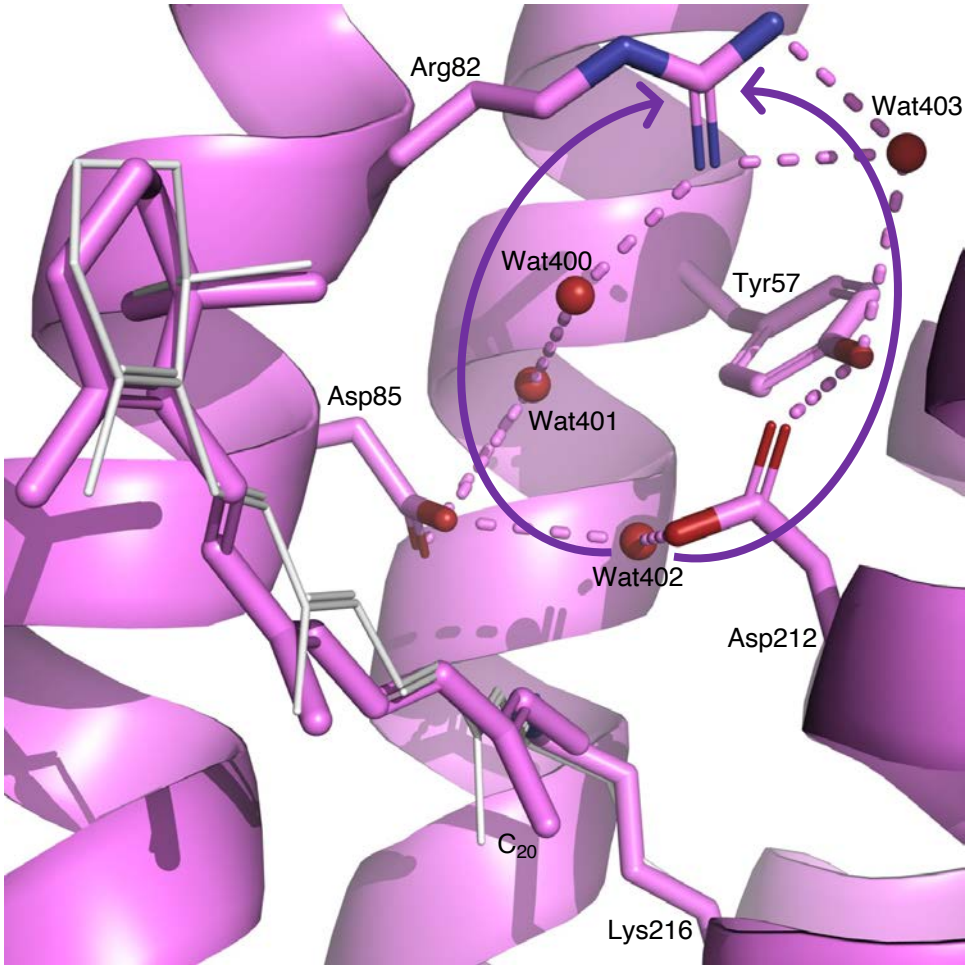

Figure S14. H-bond network at end of EC half channel in I state. Two curved arrows mark two possible proton conductance pathways. At more acidic EC pH, the pathway through Asp85 is in use and that through Asp212 is blocked by Tyr57. At more alkaline EC pH, Tyr57 could deprotonate thus the pathway through Asp212 may help to increase the proton flow. Both pathways conduct protons only under a concentration gradient of protons.

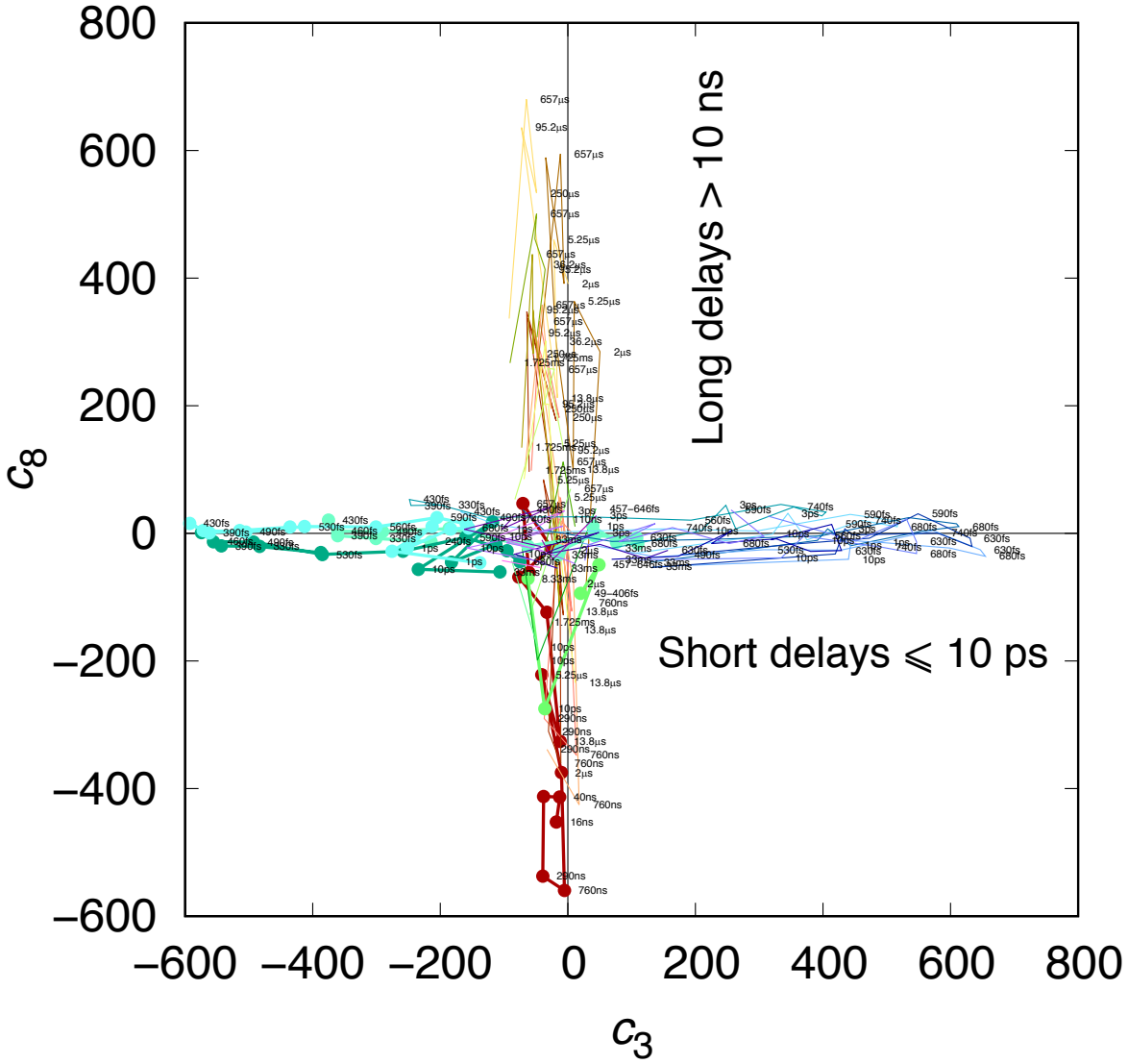

Figure S15. Short and long delays in two orthogonal subspaces. A preliminary SVD analysis shows that the difference Fourier maps at short and long delays do not share common features among the major components. This is an example to show that the third and eighth components are in two orthogonal subspaces. Each colored trace represents difference maps in a time series calculated with a common reference. Those time series with a dark reference are plotted in thick lines with dots. Other series are in thin lines without dots. Short delays are in cool colors and long delays are in warm colors.